Geothermics 66 (2017) 156–173

Contents lists available at ScienceDirect

Geothermics

journal homepage: www.elsevier.com/locate/geothermics

Fault-controlled development of shallow hydrothermal systems: Structural and mineralogical insights from the Southern Andes

Tomás Roquer[a,b], Gloria Arancibia[a,b,*], Julie Rowland[c], Pablo Iturrieta[a,b], Diego Morata[b,d], José Cembrano[a,b]

[a] Department of Structural and Geotechnical Engineering, Pontificia Universidad Católica de Chile, Santiago, Chile
[b] Andean Geothermal Center of Excellence (CEGA, FONDAP-CONICYT), Universidad de Chile, Santiago, Chile
[c] School of Environment, The University of Auckland, Auckland, New Zealand
[d] Department of Geology, Facultad de Ciencias Físicas y Matemáticas, Universidad de Chile, Santiago, Chile

ARTICLE INFO

Article history:
Received 4 January 2016
Received in revised form 8 December 2016
Accepted 8 December 2016
Available online 31 December 2016

Keywords:
Liquiñe-Ofqui Fault System
Andean Transverse Faults
Mode of failure
Zeolites
Fluid overpressure
Geothermal system

ABSTRACT

Paleofluid-transporting systems can be recognized as meshes of fracture-filled veins in eroded zones of extinct hydrothermal systems. Here we combined meso-microstructural analysis of 107 fractures and mechanical modeling from two exhumed exposures of the faults governing regional tectonics of the Southern Andes: the Liquiñe-Ofqui Fault System (LOFS) and the Andean Transverse Faults (ATF). The ATF specific segment shows two tectonic solutions that can be modeled as Andersonian and non-Andersonian tectonic regimes: (1) shear (mode II/III) failure occurs at differential stresses > 28 MPa and fluid pressures < 40–80% lithostatic in the Andersonian regime; and (2) sporadic hybrid extensional + shear (modes I + II/III) failure occurs at differential stresses < 20 MPa and anomalously high fluid pressures > 85–98% lithostatic in the non-Andersonian regime. Additionally, the LOFS exposure cyclically fails in extension (mode I) or extension + shear (modes I + II/III) in the Andersonian regime, at differential stresses < 28 MPa and fluid pressures > 40–80% lithostatic. In areas of spatial interaction between ATF and LOFS, these conditions might favor: (1) the storage of overpressured fluids in hydrothermal systems associated with the ATF faults, and (2) continuous fluid flow through vertical conduits in the LOFS faults. These observations suggest that such intersections are highly probable places for concentrated hydrothermal activity, which must be taken into consideration for further geothermal exploration.

1. Introduction

The generation and reactivation of geological faults and fracture networks creates and destroys permeability within the Earth's crust (e.g. Faulkner et al., 2010 and references therein). Fault zone permeability influences the spatial distribution and behavior of hydrothermal and geothermal systems at all scales (e.g. Krupp and Seward, 1987; Cole, 1990; Rowland and Simmons, 2012).

From the point of view of its architecture, a brittle fault zone is composed of a core surrounded by a damage zone. The core (simple or multiple) is the volume of rock in which most of the strain is accommodated, whereas the damage zone (symmetrical or asymmetrical) is the volume of rock surrounding the core, in which hydrothermally-filled fractures may occur (e.g. Faulkner et al., 2003; Sibson, 2003).

Fault-driven fluid discharge depends on the macroscopic mode of brittle failure: extension (mode I), shear (mode II/III) and hybrid extension + shear (modes I + II/III) (e.g. Sibson, 1998; Cox, 2010). Extensional (mode I) failure occurs when open fractures are formed orthogonal to the least principal stress σ_3. Shear failure (mode II/III or faulting) takes place when a movement parallel to the fracture boundary occurs. Hybrid extensional + shear (modes I + II/III) failure involves the two previous kinds of failure.

The mode of brittle failure depends on three parameters (Hubbert and Rubey, 1959; Secor, 1965): the pore fluid pressure (P_F), the differential stress (σ_1-σ_3), and the tensile strength (T). The prevailing effective stress field ($\sigma_1' = \sigma_1 - P_F > \sigma_2' = \sigma_2 - P_F > \sigma_3' = \sigma_3 - P_F$) is related to the vertical stress (σ_V) by means of the pore fluid factor (λ), which can be defined as:

$$\lambda = \frac{P_F}{\sigma_V} \quad (1)$$

* Corresponding author at: Department of Structural and Geotechnical Engineering, Pontificia Universidad Católica de Chile, Santiago, Chile.
E-mail address: garancibia@ing.puc.cl (G. Arancibia).

http://dx.doi.org/10.1016/j.geothermics.2016.12.003
0375-6505/

Where λ represents the proportion of total fluid pressure into lithostatic pressure. A value λ ~ 0.4 (40% of lithostatic pressure) is known as hydrostatic, and relates to a fault zone connected to the surface by a water column. This value is obtained by dividing the weight of the water column to the rock column. A value λ ~ 1 (100% of lithostatic pressure) is known as lithostatic, and represents a fault zone in which the values of fluid pressure equal the overburden pressure (e.g. Sibson, 2004).

The combined effect of pore fluid factors, differential stress and tensile strength on the failure mode can be conveniently represented in a pore fluid factor – differential stress space (Cox, 2010). Failure envelopes in λ – σ space are excellent graphical representations that can be used to illuminate the role of fluid pressure conditions and differential stresses in failure and permeability enhancement. In these graphs, red lines indicate extensional (mode I) failure; green lines, extensional + shear (modes I + II/III) failure; and blue lines, shear (mode II/III) failure (Fig. 1).

The rock will fail in the corresponding failure mode only when pore fluid factors and differential stresses reach the envelope. Below the envelope, the rock is elastically loaded, but will not fail. Pore fluid factors and differential stresses above the envelope are not possible. Cox (2010) provided the theoretical framework necessary to construct λ – σ failure diagrams in an intact rock or cohesion-less fault using three assumptions: (1) one of the principal stresses acts in the vertical direction (following Anderson, 1905), i.e. stresses are said to be *Andersonian*; (2) the medium principal stress σ_2 lies on the fracture plane, and therefore does not influence faulting (following Jaeger and Cook, 1979); and (3) σ_V remains constant and equals the overburden pressure. However, natural fault zones can display extreme geometrical complexity, which makes the first and second assumptions not necessarily true (cf. Hafner, 1951; Yin, 1989; Yin and Ranalli, 1992).

With the objective of proposing a temporal-spatial conceptual model of a fault-controlled shallow hydrothermal system, we studied two extinct paleofluid-transporting hydrothermal systems, now exposed as mineral-filled networks. These examples represent the major fault systems controlling the tectonics of the Southern Andes: the Liquiñe-Ofqui Fault System and the Andean Transverse Faults (Fig. 2). For the purposes of this work, the active Andean margin is an exceptional natural laboratory for studying the interactions between fault systems, fluid flow and tectonic state of stress mainly for 2 reasons: (1) hydrothermal systems occur in close spatial relationship with active volcanism and major seismically-active fault systems, and (2) excellent exposures can be found.

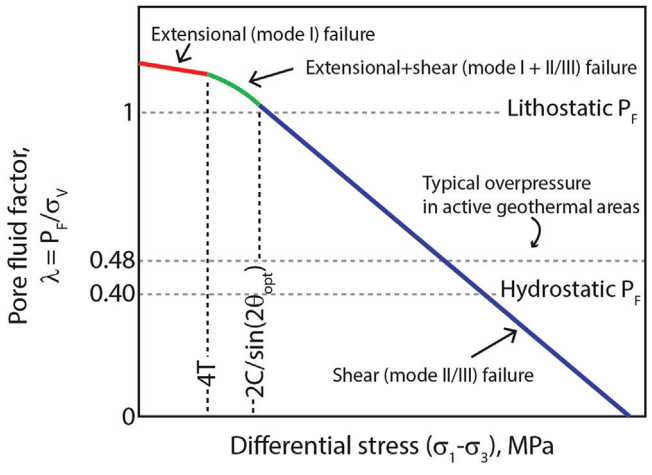

Fig. 1. Generic failure mode diagram in the λ - σ space, for a given depth and tensile strength (T) (modified from Cox, 2010). The red line indicates failure in extension (mode I); the green line, failure in extension + shear (modes I + II/III); the blue line, failure in shear (mode II/III). The rock will only fail when the pore fluid pressures and the differential stresses reach the envelope. Lithostatic and hydrostatic pore fluid factors are depicted along with typical overpressures in active geothermal areas (Rowland and Simmons, 2012). C = cohesion = 2T (Sibson, 2000), θ_{OPT} = maximum shear angle. (For interpretation of the references to colour in this figure legend, the reader is referred to the web version of this article).

Here, fluid redistribution accompanying faulting was studied using classical structural methods (field and analytical), and models of failure conditions. Field and analytical methods were used to determine the dominant modes of failure (from textural analysis) and temperature conditions (from mineral assemblages). Models of failure conditions in λ – σ space were constructed in Andersonian and non-Andersonian cases. For the non-Andersonian cases, we developed a new methodology based on the work of Cox (2010). Then, we propose the final conceptual models relating the dominant modes of failure with specific hydromechanical λ – σ conditions from mechanical calculations.

This work is a contribution to a better understanding of the still poorly documented development of fault-controlled hydrothermal systems in an Andean-type environment, which can lead to the improvement of efficient strategies for geothermal exploration in one of the largest, unexploited geothermal regions in the world.

2. Geological setting

The arc-parallel Liquiñe-Ofqui Fault System and the Andean Transverse Faults constitute the main structural features in the Southern Volcanic Zone of the Andes (33–46°S) (Lavenu and Cembrano, 1999; Rosenau et al., 2006; Sánchez et al., 2013). At least from ca. 25 Ma, these structural features have been controlled by the subduction of the Nazca and Antarctic plates beneath the South American continental plate (Somoza and Ghidella, 2005) (Fig. 2a).

2.1. Liquiñe-Ofqui Fault System (LOFS)

The LOFS is an active ca. 1200 km long Cenozoic intra-arc, strike-slip fault system. Master faults strike NS to NNE, whereas splay faults strike NE and ENE, forming strike-slip duplexes with dextral and dextral-normal movement mostly developed in the last 6 Ma (e.g. Arancibia et al., 1999; Lavenu and Cembrano, 1999; Cembrano et al., 1996; Folguera et al., 2002). The LOFS displays a kinematics compatible with strain partitioning due to the decomposition of the convergence vector: (i) NS to NNE-striking master faults accommodate the margin-parallel component, and are favorably oriented for dextral shear; and (ii) the NE to ENE subsidiary faults, in turn, are favorably oriented for dextral-transtensional to purely extensional failure (Arancibia et al., 1999; Lavenu and Cembrano, 1999; Reuther et al., 2003; Rosenau et al., 2006; Cembrano and Lara, 2009). In particular, the northernmost tip of the LOFS has been described as an active, east-branching "horse-tail" fan, with faults that strike NE, progressively becoming EW towards the east (Fig. 2a). Present-day activity of this fault system is evidenced in shallow seismic activity (< 25 km) (e.g. Lange et al., 2008).

2.2. Andean Tranverse Faults (ATF)

The ATF refer to crustal faults and morphotectonic lineaments striking oblique to the Andean orogen. These include a group of NW to WNW-striking faults identified throughout the Andes, either in the fore-arc, intra-arc and/or back-arc regions (Salfity, 1985; Cembrano and Lara, 2009; Rivera and Yáñez, 2009; amongst others). The ATF are apparently older than the LOFS, and are at least present between 25°30′–41°00′S (e.g. Taylor et al., 1998; Rivera and Cembrano, 2000; Moreno et al., 2011; Aron et al., 2010). This group of faults is probably related to the tectonic segmentation of the Andes, emplacement of NW-striking intrusive bodies, Paleozoic-Mesozoic volcanic and volcano-tectonic processes, and genesis of one or several NW to WNW-trending basins oblique to the actual

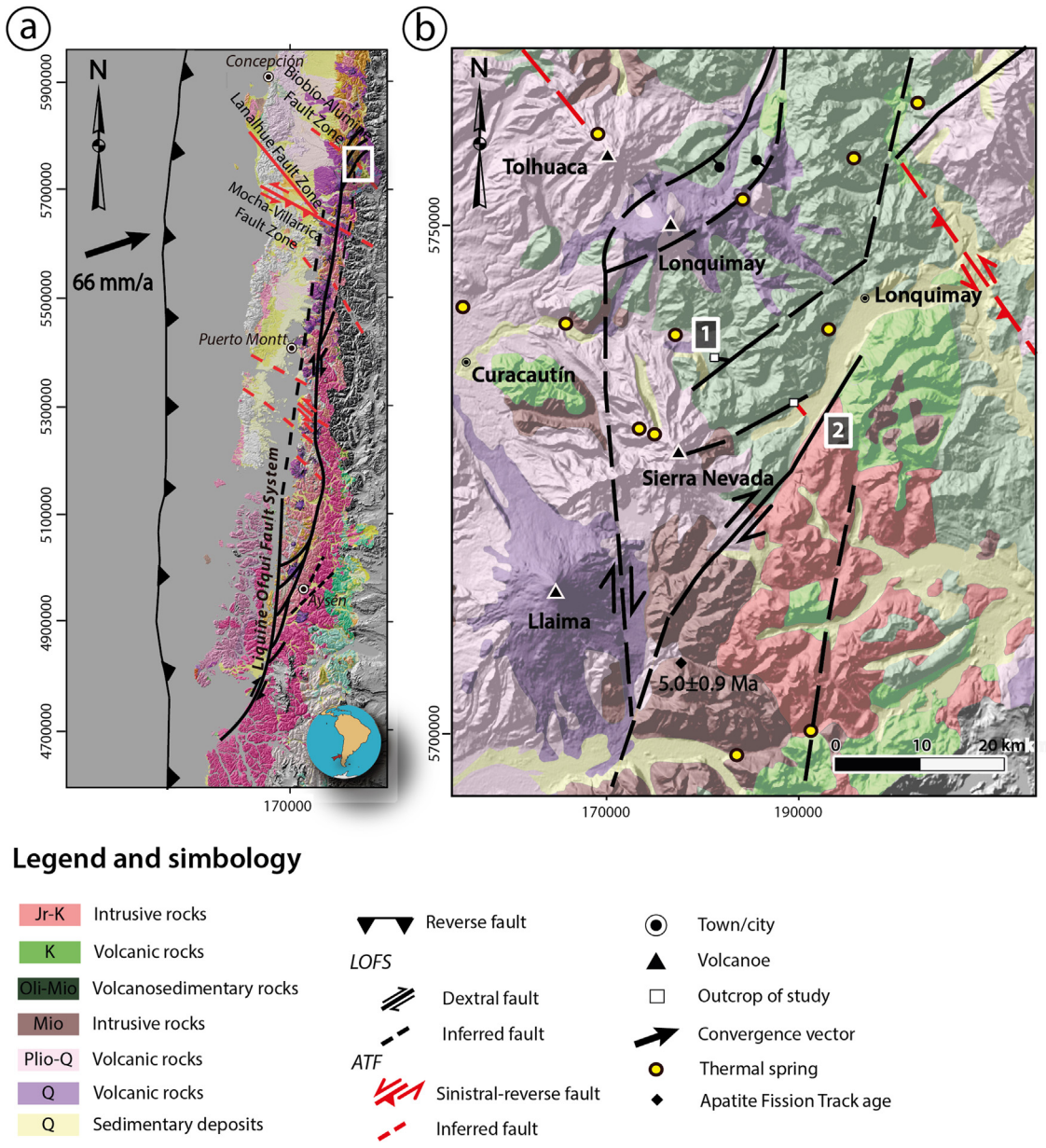

Fig. 2. a) Liquiñe-Ofqui Fault System (LOFS, black line) and Andean Transverse Faults (ATF, red line). The arrow represents the convergence vector (66 mm/a). b) Geological context of the outcrops of study, indicated in white squares as outcrops 1 (local LOFS splay fault) and 2 (ATF segment). Modified from Pérez-Flores et al. (2016). Apatite Fission Track age from Glodny et al. (2008). (For interpretation of the references to colour in this figure legend, the reader is referred to the web version of this article).

Andes, at least from the Mesozoic to the recent (e.g. Rivera and Cembrano 2000; Radic, 2010).

The seismic cycle of subduction has been proposed to play a fundamental role in the activation of the ATF (e.g. González et al., 2003; Farías et al., 2011; Aron et al., 2010; Pérez-Flores et al., 2016; Stanton-Yonge et al., 2016): (1) the interseismic period (*Andean interseismic*), in which the continental plate is under bulk compression, produces a sinistral-reverse kinematic regime; and (2) co- and postseismic period (*Andean co- and postseismic*), in which a quasi-instantaneous relaxation of upper plate is induced, transiently switches kinematics to normal-dextral.

2.3. Local geology

In the study area (ca. 38°S), the LOFS spatially and temporarily interacts with the ATF (e.g. Pérez-Flores et al., 2016). This area offers an exceptional field to study the relative role of fault systems in the formation of shallow hydrothermal systems, and consequently their control on potential geothermal reservoirs.

The studied outcrops, one of each fault system, correspond to two ca. 100-m-long sections located at about 15 km SW of the locality of Lonquimay (ca. 38°43′S) (Fig. 2b). Here, the LOFS and the ATF cut Miocene andesitic rocks, with K-Ar ages that vary between 20 and 11 Ma (Suárez and Emparan, 1988, 1995) (Fig. 2b). The andesite (Fig. 3a) has porphyritic texture with subhedral to euhedral partially albitised plagioclase phenocrysts and quartz, in a groundmass composed by tinny plagioclase microliths, quartz, magnetite, scarce pyroxene and altered volcanic glass. Secondary hydrothermal minerals fill open spaces (amygdalae and veins with chlorite) (Fig. 3b). Locally, veins bearing colorless platy crystals of zeolite cut the previously mentioned amygdalae. The oldest rocks in the study area are Jurassic monzogranites, diorites and tonalites (K-Ar ages between 148 ± 8 and 23 ± 2 Ma), and pyroclastic-andesitic Cretaceous rocks (K-Ar ages between 73.5 ± 5.0 and 13.0 ± 3.2 Ma). These

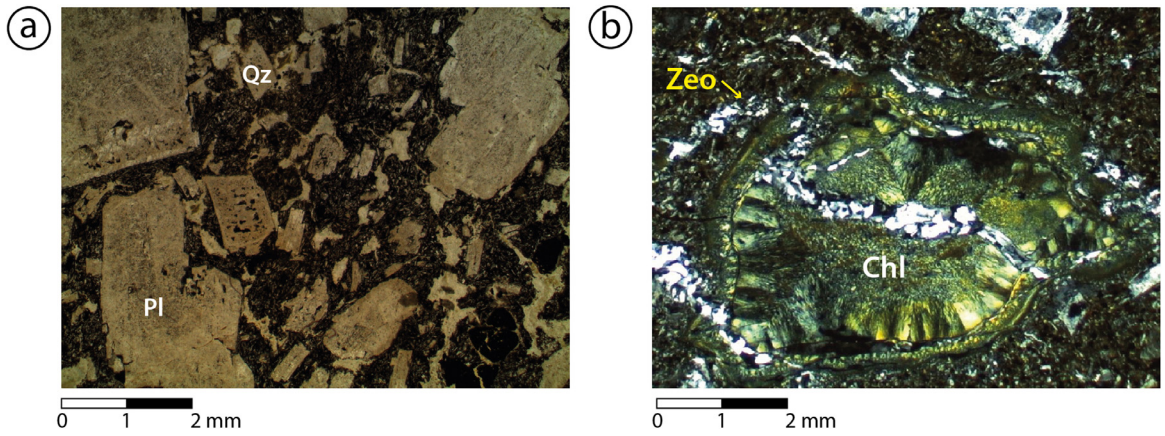

Fig. 3. Photomicrographies of: a) the andesitic host rock in the LOFS and ATF exposure; and b) hydrothermal alteration. Qz = quartz, Pl = plagioclase, Zeo = zeolite, Chl = chlorite. See text for description.

rocks are intruded by Miocene monzogranites and granodiorites (K-Ar ages between 15.2 ± 3.0 and 7.2 ± 1.9), with apatite fission track ages of 5.0 ± 0.9 Ma (Glodny et al., 2008). Above the described units there are quaternary deposits of unconsolidated, undifferentiated sediments interlayered with pyroclastic horizons (all descriptions and ages from Suárez and Emparan, 1997).

3. Methods

3.1. Field and analytical methods

Two representative outcrops in the northernmost tip of the LOFS were selected, where this system spatially and temporarily interacts with the ATF. In each outcrop, a 22-m-long transect was mapped: one of them is orthogonal to a local splay fault of the LOFS (outcrop 1 in Fig. 2b), and the other is orthogonal to a specific segment of the ATF (outcrop 2 in Fig. 2b).

Structural mapping consisted of meso- (1:50) and microscopic scale descriptions of the textures and cross-cutting relationships of discontinuities within the fault zones. Such discontinuities are here referred to as *fractures*, whose classification was based on their mesoscopic internal texture (Ramsay, 1980; Jébrak, 1997; Bons et al., 2012). These fractures include faults, veins and fault-related breccias (Peacock et al., 2016). Microstructural analysis was carried out in 3 oriented thin-polished sections of the fractures in the damage zone (oriented perpendicular to the foliation and parallel to the lineation, i.e. XZ section of the strain ellipsoid of Simpson and Schmid, 1983), and 3 samples of the isotropic host rock. Scanning electron microscopy with Energy-Dispersive X-ray spectroscopy (SEM-EDX) (Quanta 250, SEM laboratory of the CEGA-Department of Geology, Universidad de Chile) was used to obtain Backscattered Electron (BSE) images, and semi quantitative chemical analyses. Microstructural analysis of the fractures involved making 3 microstructural maps (1 fault-vein + 1 vein of the LOFS exposure, and 1 hydrothermal breccia of the ATF exposure). The construction of the microstructural maps involved the creation of a photomosaic of approximately 150 pictures per map, taken under the petrographic microscope (XPL – 2.5x). The microstructural classification of the veins within oriented samples was based on the morphology and growth direction of the crystals, being only distinguished syntaxial veins, characterized by having crystals growing out from the country rock towards a median zone, or from one boundary towards the other (e.g. Bons et al., 2012). The occurrence of a syntaxial vein was related to at least one crack-seal episode (Ramsay, 1980; Wilson, 1994). All mineral abbreviations were obtained from Whitney and Evans (2010).

X-ray diffraction (XRD) analyses were conducted in the core and the damage zone. A total of 60 samples were collected (25 of the LOFS exposure, and 35 of the ATF exposure). The hydrothermal mineral infill was separated and ground to a particle size < 10 μm to minimize possible micro-absorption effects, and to increase the accuracy of the obtained intensities. XRD analyses were performed in the Crystallography Laboratory from the Physical Department, Universidad de Chile, using a Bruker D8 Advance X-Ray Diffractometer (radiation Cu Kα = 1.5406 Å), equipped with a Cu X-Ray tube (operating at 40 kV/30 mA), Ni filter, sample spinner and a solid state detector (Lineal LynxEye). The Bragg-Brentano geometry was used. The samples were mounted in a 2 cm x 2 cm square sample holder. The resulting diffractograms were interpreted with the software package Match! by Crystal Impact, and compared with Panalytical-ICSD (Inorganic Crystal Structure Database) database.

The linear fracture density of macroscopic fractures (δ_x) was determined by calculating the ratio (e.g. Gillespie et al., 1993):

$$\delta_X = \frac{n}{L_x} \quad (2)$$

where n = number of fractures intersecting along a vertical plane perpendicular to the corresponding fault core; and L_x = length of the damage zone in the hanging or footwall block.

3.2. Failure conditions in $\lambda - \sigma$ space

Based on the work of Cox (2010) to construct a $\lambda - \sigma$ space in Andersonian regimes, we developed a new method that expands the analysis to the case where σ_2 does not lie on the fault plane, nor σ_V is equaled to any principal stress. This is the case of preexistent faults within a randomly oriented stress field. The method uses as inputs: (1) the orientation of the stress tensor and the stress tensor shape ratio ϕ; (2) mechanical properties of the host rock (tensile strength T and coefficient of internal friction μ); (3) depth level of exposure of the studied fractures; and (4) a representative orientation of such fractures. The output of the model is the pore fluid factor (λ) and differential stress (σ) for different modes of failure, at the time of fracture formation.

The mechanical fundament of this analysis is that the principal stress field can be projected on the plane of interest, which produces both a tangential and normal stress on the pre-existing surface. Governing equations of the stress projection and failure envelope construction are described in the following subsections.

3.2.1. Stress tensor algebra

Orientation of the stress tensor principal axes and the stress tensor shape ratio ϕ are used as inputs in our model, and were

Table 1
Tectonic solutions considered to model the modes of failure. σ_1 = greatest principal stress, σ_3 = least principal stress, ϕ = stress tensor shape ratio. Obtained from Pérez-Flores et al. (2016).

Tectonic solution	σ_1	σ_3	ϕ
LOFS Andersonian	N014°W/03°N	N078°E/32°E	0.2
ATF Andersonian	N110°E/19°SE	N011°E/11°N	0.6
ATF non-Andersonian	N133°W/45°SW	N004°W/32°N	0.9

obtained from the work of Pérez-Flores et al. (2016) (Table 1). These parameters were calculated using field observations from striations on fault surfaces (e.g. Yamaji, 2000).

The stress tensor is expressed in the vector basis built by the principal stress axes orientations (here after referred to as *eigenvector basis*):

$$\hat{\boldsymbol{\sigma}} = \begin{bmatrix} \sigma_1 & 0 & 0 \\ 0 & \sigma_2 & 0 \\ 0 & 0 & \sigma_3 \end{bmatrix} \tag{3}$$

The stress tensor shape ratio ϕ is the relative proportion between the magnitudes of principal stresses:

$$\phi = \frac{\sigma_2 - \sigma_3}{\sigma_1 - \sigma_3} \tag{4}$$

However, the stress tensor should be expressed in convenient basis vectors, such as the basis built by NS-EW-vertical axes (here after referred to as *geographic basis*). To transform the stress tensor from eigenvector to geographic basis, we use the tensorial transformation law:

$$\boldsymbol{\sigma} = \boldsymbol{R}\hat{\boldsymbol{\sigma}}\boldsymbol{R}^{\boldsymbol{T}} \tag{5}$$

Where $\boldsymbol{\sigma}$ is the stress tensor expressed in the geographic basis, $\hat{\sigma}$ is expressed in the eigenvector basis, and $\boldsymbol{R}$ is an orthonormal *rotation* matrix, whose columns represent the *i*-th eigenvector expressed in the geographic basis. Moreover, this rotation is defined by the direction cosines between both sets of basis vectors, which can be expressed in terms of the azimuth (α) and plunge (β) of the stress principal axes:

$$\boldsymbol{R} = \begin{bmatrix} \sin(\alpha_1)\cos(\beta_1) & \sin(\alpha_2)\cos(\beta_2) & \sin(\alpha_3)\cos(\beta_3) \\ \cos(\alpha_1)\cos(\beta_1) & \cos(\alpha_2)\cos(\beta_2) & \cos(\alpha_3)\cos(\beta_3) \\ -\sin(\beta_1) & -\sin(\beta_2) & -\sin(\beta_3) \end{bmatrix} \tag{6}$$

In this way, for a given plane with normal vector $\boldsymbol{n}$ defined in the geographic basis, we now define stress components. First, the traction vector $\mathbf{t_n}$ is the projection of the stress tensor $\boldsymbol{\sigma}$ on the plane:

$$\boldsymbol{t_n} = \boldsymbol{\sigma n} \tag{7}$$

Following, the normal stress (σ_n) is the magnitude of the projection between $\mathbf{t_n}$ and the direction of interest ($\mathbf{n}$):

$$\sigma_n = \boldsymbol{n} \cdot \boldsymbol{t_n} = \boldsymbol{n} \cdot \boldsymbol{\sigma n} \tag{8}$$

Maximum shear stress (τ) in this plane is the magnitude of the difference between those vectors:

$$\tau = |\boldsymbol{t_n} - \sigma_n \boldsymbol{n}| = \sqrt{|\boldsymbol{\sigma n}|^2 - \sigma_n^2} \tag{9}$$

We note that σ_n and τ are defined in terms of $\mathbf{n}$ and σ_i, α_i, β_i for i=1,2,3. However, we recall that α_i, β_i and $\mathbf{n}$ are known from the structural data, with σ_i as the remaining unknowns. Moreover, σ_2 can be removed of Eqs. (8) and (9) re-casting Eq. (4):

$$\sigma_2 = \phi(\sigma_1 - \sigma_3) + \sigma_3 \tag{10}$$

Hence, $\boldsymbol{\sigma}$ components are functions that use only σ_1 and σ_3 as arguments. Given that the stress tensor is expressed in the geographic basis, σ_V is found within the $\hat{e}_3$ direction of the basis, therefore represented by the (3,3) component of $\boldsymbol{\sigma}$:

$$\sigma_V = \sigma_{33} = \hat{\boldsymbol{e}}_3 \cdot \boldsymbol{\sigma}\hat{\boldsymbol{e}}_3 = \rho g z \tag{11}$$

Where ρ is the rock density, g the gravity constant and z the depth of analysis. Using equation (5) and some algebra in equation (11), we express the vertical pressure in terms of the principal stresses:

$$\hat{\boldsymbol{e}}_3 \cdot R\hat{\sigma}R^T\hat{\boldsymbol{e}}_3 = \rho g z \tag{12}$$

$$\sigma_1 \sin^2\beta_1 + \sigma_2 \sin^2\beta_2 + \sigma_3 \sin^2\beta_3 = \rho g z \tag{13}$$

Finally, we remove σ_2 using equation (10):

$$\sigma_1(\sin^2\beta_1 + \phi\sin^2\beta_2) + \sigma_3\left(\sin^2\beta_3 + (1-\phi)\sin^2\beta_2\right) = \rho g z \tag{14}$$

On the other hand, we recall that the differential stress σ is given by the equation:

$$\sigma = \sigma_1 - \sigma_3 \tag{15}$$

Substituting Eq. (15) in Eq. (14) we obtain the principal stresses in function of σ and z:

$$\sigma_1 = \frac{\rho g z + \sigma\left[\sin^2\beta_3 + (1-\phi)\sin^2\beta_2\right]}{\sin^2\beta_1 + \sin^2\beta_2 + \sin^2\beta_3} \tag{16}$$

$$\sigma_2 = \frac{\rho g z + \sigma\left[(\phi-1)\sin^2\beta_1 + \phi\sin^2\beta_3\right]}{\sin^2\beta_1 + \sin^2\beta_2 + \sin^2\beta_3} \tag{17}$$

$$\sigma_3 = \frac{\rho g z - \sigma\left[\sin^2\beta_1 + \phi\sin^2\beta_2\right]}{\sin^2\beta_1 + \sin^2\beta_2 + \sin^2\beta_3} \tag{18}$$

Consequently, for a given σ and z, the values of σ_n and τ are obtained using Eqs. (8) and (9), which allows us to produce failure envelopes in terms of σ and λ.

3.2.2. *Failure criteria in $\lambda - \sigma$ space*

Three failure criteria are commonly used in rock mechanics for brittle failure, which depend on the mode of fracture. The first is extensional (mode I), which implies σ_n is lower than −T, the tensile strength of the rock. Moreover, for fracture development, the plane orientation is orthogonal to σ_3, thus $\sigma_n = \sigma_3 < -T$. However, when σ_1 and σ_2 do not lie on the fault plane (or generally when less than any two principal stress directions), *shear stress will always be present*. This can be illustrated by the 3D Mohr's circle (Fig. 4a). The following two criteria are hybrid extensional + shear (modes I + II/III) failure and pure shear (mode II/III) failure, which are well constrained by the Griffith and the Mohr-Coulomb failure envelopes, respectively.

Therefore, extension (mode I) criteria can be only applicable to the cases when the rock is subjected to an isotropic tensile state of stress, to fracture development or to preexistent faults in optimal orientation (parallel to both σ_1 and σ_2). In this analysis, which is extended for cases different from the above mentioned, we use the Murrel's expansion of Griffith criterion (generalized Griffith criterion) to constrain the case of hybrid extension + shear (modes I + II/III):

$$\tau^2 = 4T\sigma_n' + 4T^2 \tag{19}$$

Where σ_n' is the effective normal stress ($\sigma_n' = \sigma_n - P_F$). This parabolic criterion retrieves both shapes of extension (mode I) and extension + shear (modes I + II/III) envelopes when subjected to an Andersonian regime with σ_2 lying on the fault plane. Finally, shear

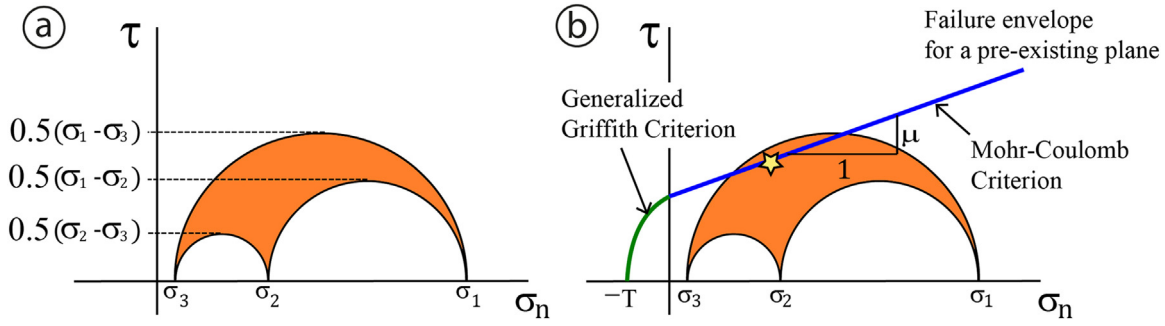

Fig. 4. a) 3D Mohr's circle, representing a random tri-axial state of stress. Each circle represents the state of stress within planes containing two principal stresses. The radiuses of the circles represent the maximum shear stress within such plane. However, the stress state of a plane oblique to all three principal stresses is located within the shaded area. Graphically, the only possibility to have zero shear stress is to be located within a plane, whose normal is parallel to any principal direction. b) Failure envelope for a preexistent plane within a random tri-axial state of stress. Extension + shear (modes I + II/III) is described by the Generalized Griffith criterion (green), whereas pure shear (mode II/III) by the Mohr-Coulomb criterion (blue). The greater circle does not necessarily contain the failure plane, but rather a preexistent plane in the shaded area if intersected by the failure envelope (yellow star). (For interpretation of the references to colour in this figure legend, the reader is referred to the web version of this article).

(mode II/III) failure is described by using the Mohr-Coulomb criterion (both criterions are illustrated in Fig. 4b):

$$\tau = \mu\sigma_n^{'} + c \tag{20}$$

Which involves the fault friction coefficient μ and cohesion c. To construct failure criterion in the $\lambda - \sigma$ space, we substitute normal effective stress in terms of total stress and pore fluid pressure:

$$\sigma_n^{'} = \sigma_n - P_F \tag{21}$$

Then, replacing equation (21) into equations (19) and (20), and dividing by σ_V, we obtain failure envelopes in terms of the pore fluid factor λ:

$$\lambda = \frac{P_f}{\sigma_V} = \frac{\sigma_n + T}{\sigma_V} + \frac{\tau^2}{4T\sigma_V} \tag{22}$$

$$\lambda = \frac{P_f}{\sigma_V} = \frac{\sigma_n}{\sigma_V} + \frac{c - \tau}{\mu\sigma_V} \tag{23}$$

We recall that σ_n, σ_V and τ are defined in terms of σ_1 and σ_3 (as indicated in Eqs. (8), (9) and (13)), which are calculated using a given differential stress σ and depth z. Thus, we can obtain the required λ for failure using the Griffith criterion (Eq. (19)) or Mohr-Coulomb (Eq. (20)) in the $\lambda - \sigma$ space. These failure criteria are delimited when σ_n is positive (Mohr-Coulomb) or negative (generalized Griffith criterion).

A similar approach to obtain fluid pressures has been used by Hashimoto and Eida (2015), where pore pressure factors are calculated for vein development in an accretionary complex. Using the multiple inverse method for stress inversion (and therefore non-Andersonian regimes), they calculated τ and σ_n for all planes corresponding to the vein elements identified, using a normalized Mohr's circle (differential stress $\sigma_1 = 1$ and $\sigma_3 = 0$). Following, effective friction coefficient is obtained from the slope between critically loaded vein planes in the normalized Mohr's circle (both veins with the minimum and maximum slip tendency, $T_s = \frac{\tau}{\sigma_n}$) (following Morris et al., 1996), by using a non-cohesive Mohr-Coulomb failure criteria. Finally, pore pressure factors are calculated from the analytical theory of Coulomb wedges (Dahlen, 1984), depending inversely of the effective friction coefficient. However, we argue that the method presented here is more representative of fracture-vein systems development. In this work, the structural data used for stress inversion is entirely different of the vein system upon which the pore pressure analysis was undertaken. Therefore, any recursive inference is avoided. On the other hand, cohesion must be considered in failure analysis, especially given the significance of healing processes in hydrothermal systems (Tenthorey et al., 2003). Moreover, as presented in this work, textural analysis evidences not only the existence of shear (mode II/III) failure, but extension (mode I) and hybrid (modes I + II/III) failure also, implying that other failure criteria rather than Mohr-Coulomb must be used to capture these failure mechanisms (such as generalized Griffith). Finally, considering an average orientation of a fracture-vein system, as done here, may lead to a better approximation of pore fluid factors, in opposite to defining two end-members of the data set, which is rather sensitive to the choice of the critically loaded fractures.

4. Results

4.1. Fault zone architecture and fractures within the damage zones

A total of 107 fractures occurring in the studied damage zones were analyzed. Fractures in the damage zones consist of secondary structures having or not a hydrothermal filling. Five families of fractures were identified in the studied fault zones (Figs. 5–6): (1) hydrothermal breccia; (2) fault-localized hydrothermal breccia; (3) vein; (4) fault-vein; and (5) fault. All of these fractures have tabular shape, width/length ratio < 0.001 and most are associated with zeolite precipitation (Fig. 6a–e). The different fractures are texturally described as following:

Hydrothermal breccia: These fractures are composed of subangular clasts of the host rock and/or hydrothermal clasts, in a fine matrix of hydrothermal minerals (Fig. 6a).

Fault-localized hydrothermal breccia: These fractures are composed of two different bands: (1) one or more hydrothermal breccias that are contained in (2) a tectonic comminution breccia (Fig. 6b). The hydrothermal breccia band is composed of two populations of subangular clast, interpreted to be from the host rock and previously precipitated hydrothermal minerals, and a fine-grained zeolitic matrix. The fault breccia band (cut by the hydrothermal breccia band), has foliated cataclastic fabric with S-C internal structure, consistent with reverse movement.

Vein: These fractures have hydrothermal infill, with no evidence of internal shear (mode II/III) (Fig. 6c). Veins are filled with equant milimetric crystals, without any preferred orientation on observation under naked eye.

Fault-vein: These fractures show evidence of shear (mode II/III) and growth of hydrothermal minerals (Fig. 6d).

Fault: These fractures show evidence for shear (mode II/III) (i.e. striae), but no hydrothermal infill (Fig. 6e).

4.1.1. LOFS splay fault

From an architectural point of view, the LOFS outcrop has a simple core and an asymmetric damage zone, with a higher fracture

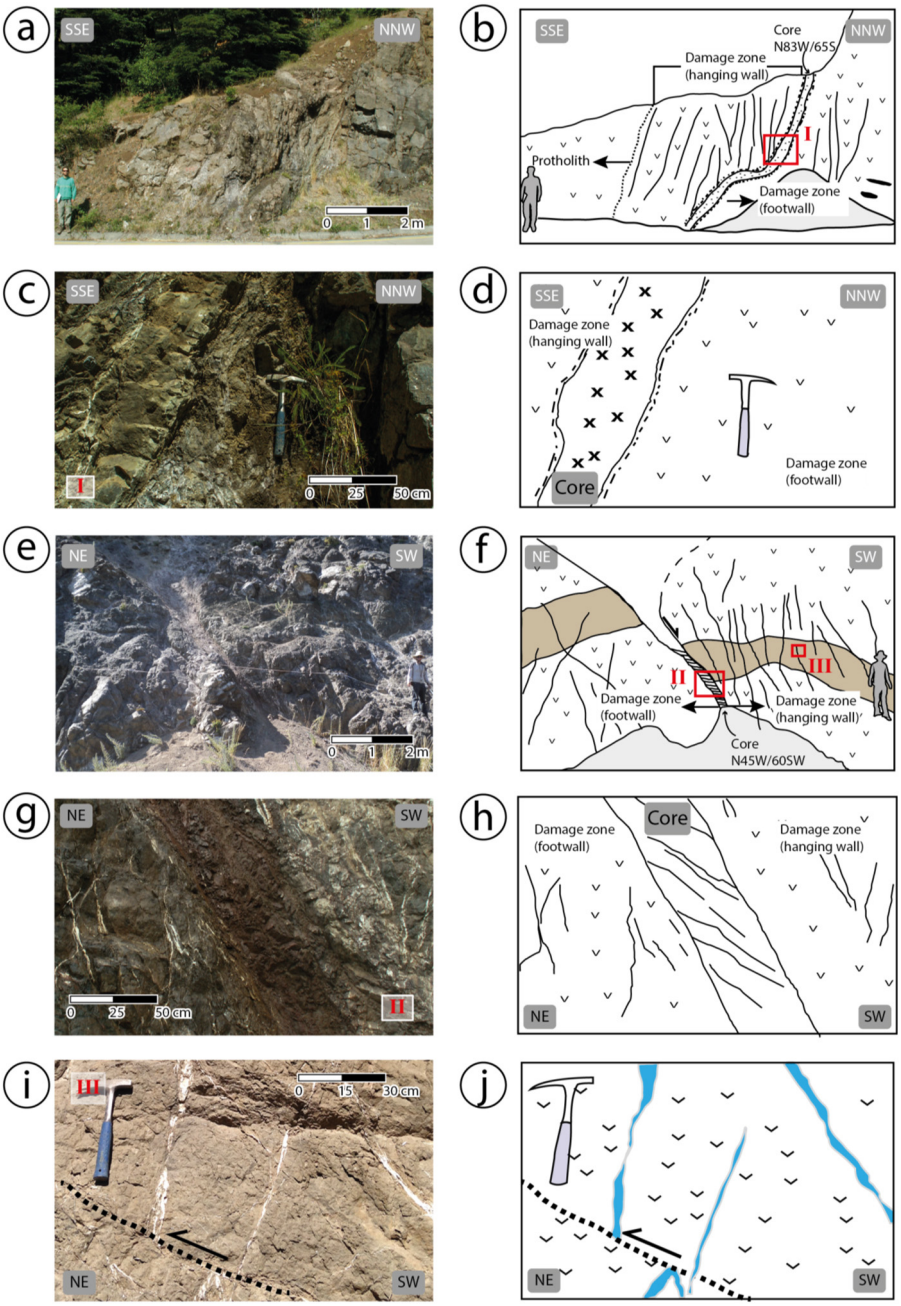

Fig. 5. a) Photography of the studied splay fault of the LOFS (cross section, picture looking to the WSW). b) Cartoon of the LOFS exposure, showing the fault core (microdioritic dyke with fault gouge in its borders), the damage zone (dominated by NNE-ENE/subvertical fractures) and the protolith. c) Photography of the LOFS splay fault core (picture looking to the WSW). d) Cartoon of the core of LOFS exposure. e) Photography of the studied segment of the ATF (cross section, picture looking to the SE). f) Cartoon of the ATF exposure, showing the fault core (foliated gouge consistent with normal movement) and the damage zone (dominated by NW/subvertical fractures). g) Photography of the core of the studied ATF exposure (cross section, picture looking to the SE). h) Cartoon of the core of ATF exposure. i) Example of NW/gently dipping faults cutting and separating NW/subvertical fractures (cross section, picture looking to the SE). j) Cartoon of NW/gently dipping fault.

density in the hanging wall (4.80 fractures/m), than in the footwall (1.51 fractures/m) (Fig. 5a, b). The N83°W/65°SW core has a width of 0.4 m, and is composed of a microdioritic dyke with local fault gouge and banded vein in its borders (zone I in Fig. 5a–d). Damage zone in the hanging wall extends 5 m away from the core to the SSE, whereas in the footwall extends for 15 m to the NNW.

The detailed description of occurring fractures is the following:

a) Hydrothermal breccia (n = 16)

Hydrothermal breccias are present in both the footwall and the hanging wall, and have widths on the cm-scale, with along dip continuity > 5m. The hydrothermal breccia bodies strike between NNE and ENE, and dip steeply to the S. Some of these elements exhibit kinematic indicators of dextral and dextral-normal displacement, with rakes < 30° from the NE.

b) Vein (n = 11)

Veins occur in the hanging wall and the footwall blocks, and locally occur as banded aggregates. Vein widths vary from mm-to-cm scale, with along dip continuity > 5m. Most of the veins are N50–60°E/subvertical structures.

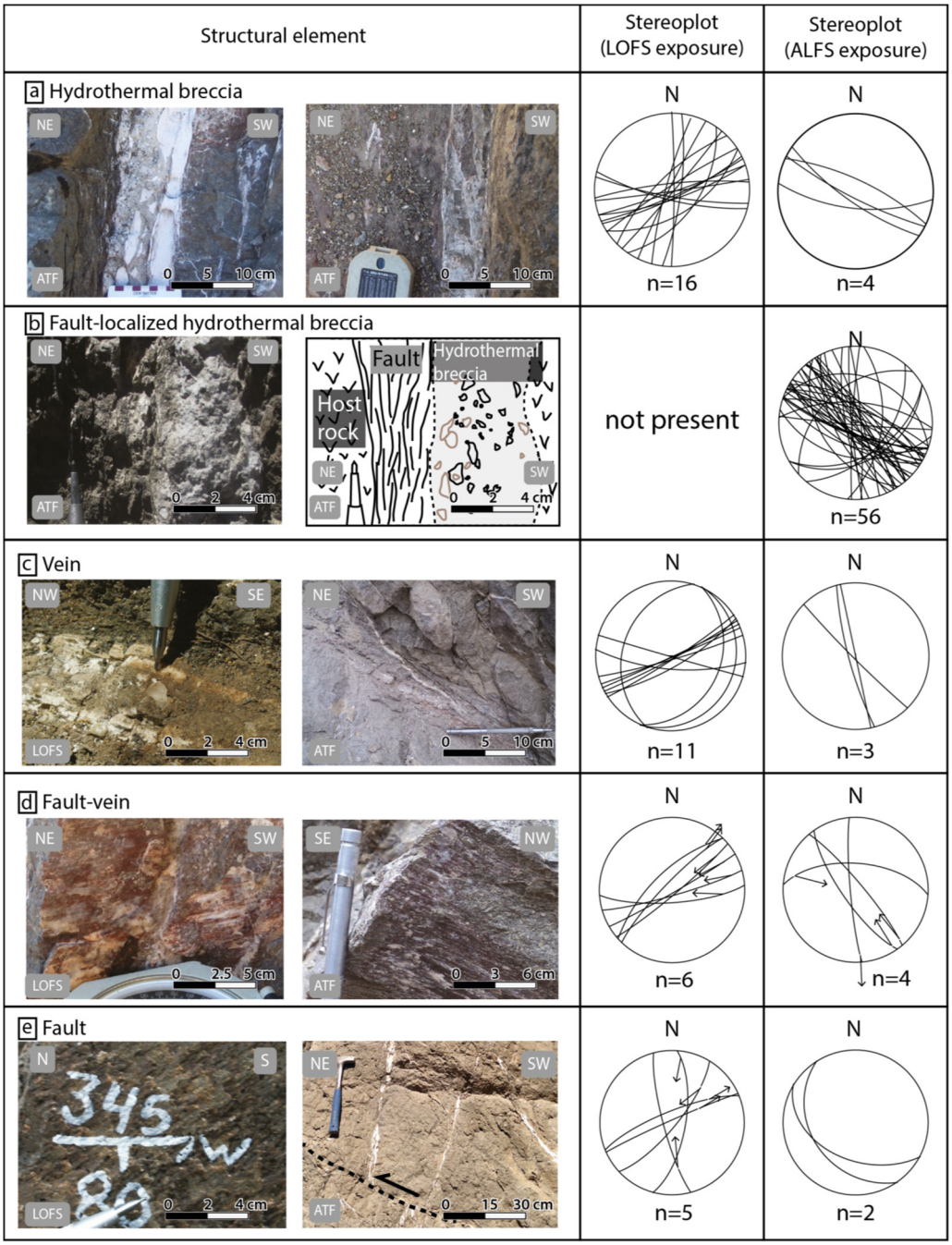

Fig. 6. Left, examples of the fractures occurring in the LOFS and the ATF exposures. Right, geometry of the fractures. a) Hydrothermal breccias are here defined as any fracture that has clasts cemented by a hydrothermal matrix (pictures are cross sections, looking to the SE). b) Fault-localized hydrothermal breccia is distinguished from hydrothermal breccia since the latter is contained in a cm-to-mm width fracture with cataclastic fabric, as shown in the cartoon to the right of the picture (picture is a cross sections, looking to the SE). c) Veins are filled of equant milimetric crystals without any preferred orientation (picture to the left is a plan view, picture to the right is a cross section, looking to the SE). d) Fault-veins are here defined as fractures with evidence internal shear and mineral precipitation (mainly quartz and calcite) (pictures are cross sections, picture to the left, looking to the SW; picture to the right looking to the SE). e) Faults are slip surfaces with no mineral precipitation (picture is a cross section, looking to the E). Arrows on the stereoplots indicate the sense of movement of the hanging wall block. All stereograms are lower-hemisphere equal-area projections.

c) Fault-vein (n = 6)

Fault-veins are exclusively found in the hanging wall. The fault-veins in this outcrop have widths on the mm-scale, and persist > 0.5 m along dip. The kinematics of opening is recorded by the presence of quartz or calcite mineral fibers. Two families of vein-faults were distinguished: dextral-reverse N65–90°E/80°S, and dextral-normal N40–45°/80°N, both families with rakes 15–20° from the E. Cross-cutting relationships between them could not be determined.

d) Fault (n = 5)

Faults occur in both the footwall and the hanging wall blocks. These slip surfaces are exposed in patches of several tens of square centimeters, and have a preferred NE-striking/subvertical attitude. The rakes are < 35° from the NE, indicating dextral-reverse movement principally recorded in steps.

4.1.2. ATF specific segment

The ATF outcrop (Fig. 5e, f) exhibits a simple core and an asymmetric damage zone. Fracture density within the hanging wall block (3.53 fractures/m) is greater than in the footwall (2.18 fractures/m). The N45°W/60°SW core has a width of 0.5 m, and consists of foliated gouge with S-C internal structure consistent with normal movement (zone II in Fig. 5e–h). Damage zone in the hanging wall extends 15 m away from the core to the SW, whereas in the footwall extends 5 m to the NE.

The detailed description of occurring fractures is the following:

a) Hydrothermal breccia (n = 4)

Hydrothermal breccias are concentrated in the hanging wall, display width on the centimetric scale and along dip continuity > 5m. These elements show a preferred WNW-striking, high angle dipping to the S attitude.

b) Fault-localized hydrothermal breccia (n = 56)

Fault-localized hydrothermal breccias only occur in the ATF exposure, and are concentrated in the hanging wall block. These fractures exhibit widths on the cm-scale, with along dip continuity > 5 m. The boundaries of the breccia bodies strike preferentially N40–50°W, with high angle dips to the SW. Some of these structures exhibit evidence of reverse shear, as inferred from obliquity of the foliation with respect to the boundaries. Fault-localized hydrothermal breccias in this outcrop locally cut and are cut by NW-striking, gently dipping faults with reverse centimetric separation (zone III in Fig. 5e–f,i–j).

c) Vein (n = 3)

Veins only occur in the footwall, and presented cm-to-mm widths with continuity along dip between 0.5-5.0 m. NW to NNW strikes with high angle dips are dominant.

d) Fault-vein (n = 4)

Fault-veins are present in both the footwall and hanging wall. The vein-faults in this outcrop have mm-scale widths, and persist for about 0.5 m along dip. They are preferentially sinistral N5−45°W/subvertical surfaces with rakes < 10° from the S and the E.

e) Fault (n = 2)

Faults occur in the hanging wall block, and have widths ca. 1–2 cm and along-dip continuity > 1.5 m. Faults in this outcrop have preferred N40–50°W/25–30°S attitude, and cut and are cut by fault-localized hydrothermal breccias, which exhibit reverse separation on the cm-scale (zone III in Fig. 5e–f, i–j). Rakes could not be determined with the mesostructural analysis.

4.2. Mineral identification using X-ray powder diffraction

The previously described fractures are dominated by zeolitic assemblages in both exposures, from which stability temperature intervals may be obtained (*e.g.* Kristmannsdóttir and Tómasson, 1978; Liou et al., 1987). The prevalent zeolite is laumontite, whereas other zeolites such as yugawaralite, heulandite, natrolite, scolecite, stilbite, chabacite and wairakite also are present. Common hydrothermal minerals, such as quartz and calcite also occur.

4.2.1. LOFS splay fault

The LOFS exposure has laumontite, quartz, stilbite and calcite as the prominent minerals, distributed in the core and the damage zone (Fig. 7). In this exposure, the assemblage laumontite + stilbite is dominant along the fault zone (e.g. Fig. 8a). Minor quartz, calcite and chabacite were also locally found.

4.2.2. ATF specific segment

In the ATF segment laumontite is the dominant hydrothermal mineral, and is uniformly distributed within the core and the damage zone (Fig. 7). Natrolite and quartz were detected in the core as well as in both sides of the damage zone, close to the core. Scolecite, stilbite, chabacite and heulandite were only found in the hanging wall. Calcite was only detected in one sample. Pyroxene, feldspar and mica, coming from the andesitic host rock, are restricted to the hanging wall. In the ATF outcrop no dominant mineral assemblages were detected, but in the damage zone two associations are locally present: laumontite + scolecite (e.g. Fig. 8b) and laumontite + wairakite (e.g. Fig. 8c).

4.3. Microstructural analysis

The detailed description of the microstructural maps is shown in the following subsections.

4.3.1. Fault-vein of the LOFS splay fault

The chosen representative NNE-striking sample of a fault-vein in the LOFS outcrop, found in the hanging wall block, has a width varying from 0.5 cm to 1.0 cm, with a diffuse and curved contact with the andesitic host rock (Fig. 9a, b). The hydrothermal filling in this sample is composed of three microstructural families, distinguished by their orientation (identified in green in Fig. 9b): (1) a NE-striking *en-échelon* array of lenticular veins filled with platy-elongate and relatively large crystals of subhedral-euhedral laumontite (0.15–0.50 mm) (zone II in Fig. 9b, c); (2) a

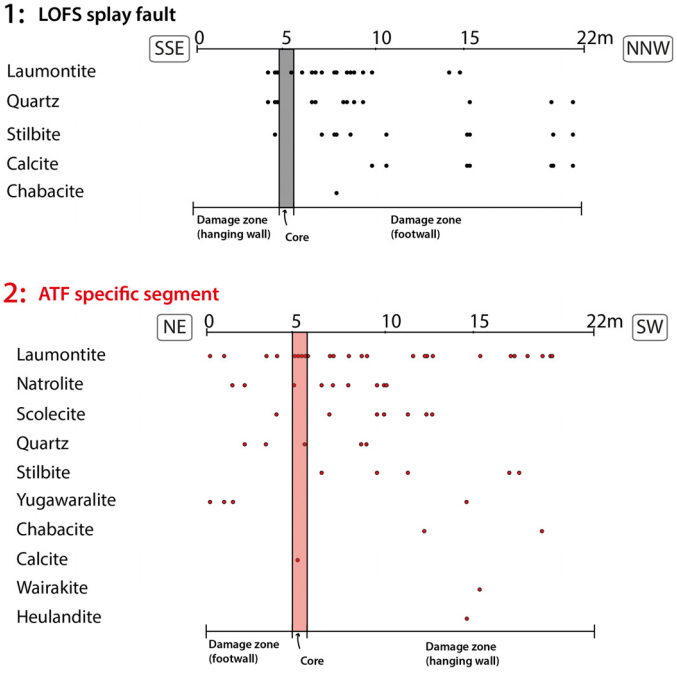

Fig. 7. Spatial distribution of the syntectonic hydrothermal mineralogy present in the LOFS (black dots) and the ATF (red dots) exposures. The cores are shaded, and the position of the damage zones is also indicated. See text for description. (For interpretation of the references to colour in this figure legend, the reader is referred to the web version of this article).

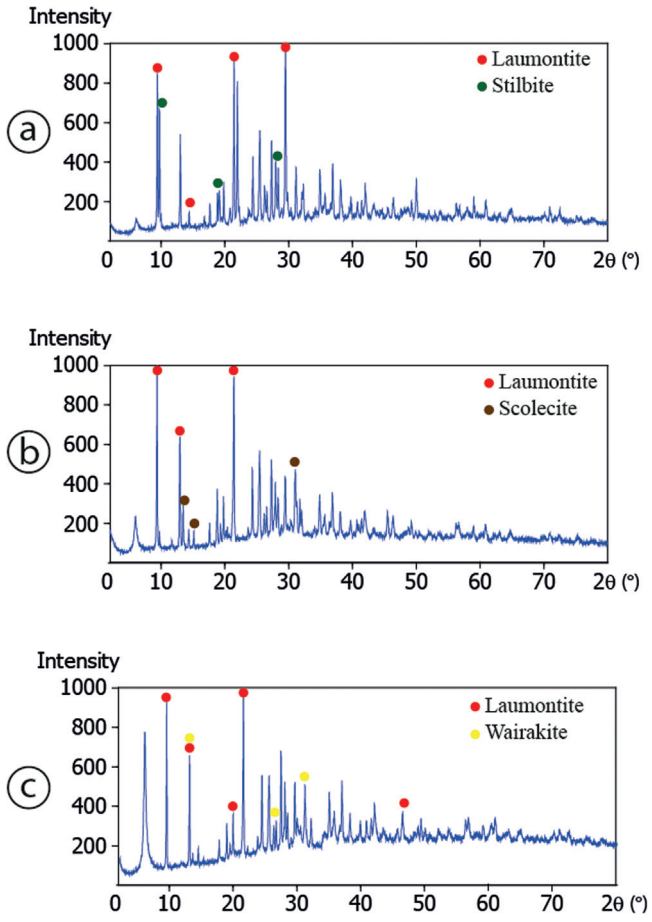

Fig. 8. Examples of interpreted diffractograms: a) Association laumontite + stilbite (sample LR8.4–LOFS exposure); b) Association laumontite + scolecite (sample LAZI12.83–ATF exposure); c) Association laumontite + wairakite (sample LR15.52–ATF exposure). Colored dots indicate the strongest peaks of corresponding mineral phases: red = laumontite; green = stilbite; brown = scolecite; yellow = wairakite. (For interpretation of the references to colour in this figure legend, the reader is referred to the web version of this article).

cataclastic fine-grained mixture of subangular clasts of laumontite (0.05–0.25 mm) embedded in a matrix of iron oxide (zone I in Fig. 9b, c), that occurs between the NE-striking lenticular fractures or as NNE-striking bands, and (3) a ENE-striking family of fractures, filled with a mosaic of subhedral-platy laumontite (0.05–0.10 mm).

The NE-striking *en-échelon* lenticular veins occur in two NNE-striking bands (bands A and B in Fig. 9b), distinguished by dominant size of single veins in the corresponding band (characteristic sizes: 10 mm × 5 mm in band A and 2.5 mm × 1.5 mm in band B). Individual lenticular veins have small equant crystals of laumontite: (1) concentrated in the two boundaries, with increasing length/width ratio towards a median zone (zone II in Fig. 9b, c); or (2) concentrated in one boundary increasing the length/width ratio towards the opposite boundary. In both cases, the long axis of the crystals is oriented perpendicular to the boundaries, which is consistent with syntaxial growth and at least one crack-seal episode (Ramsay, 1980; Wilson, 1994; Bons et al., 2012).

On the other hand, the fine-grained cataclastic unit, which occurs between the NE-striking lenticular fractures or as NNE-striking bands, is composed of angular clasts (40%) with iron oxides as matrix (60%) (zone I in Fig. 9b, c). According to the classification of Woodcock and Mort (2008), such rock can be classified as a cataclasite.

Two key observations can be made: (i) the median zone in the NE-striking lenticular veins locally exhibits cataclastic texture (zone III in Fig. 9c), and (ii) the cataclastic bands have laumontite clasts (zone I in Fig. 9c). Both textures suggest that the NNE-striking *en-échelon* array of NE-lenticular veins served as a zone of weakness that localized extension and dextral shear, as inferred from the obliquity of lenticular veins with respect to the contact with the host rock. This inference is consistent with proposed models on the formation of *en-échelon* veins (e.g. Olson and Pollard, 1991).

4.3.2. Vein of the LOFS splay fault

The sample of the vein, within the footwall, and in contact with the fault core in the LOFS outcrop, is composed by three parallel EW-striking bands (bands A, B and C in Fig. 10a, b), all filled with an aggregate of laumontite + stilbite and calcite. These bands are distinguished by the size of the crystals of the laumontite + stilbite aggregate: bands A and C are relatively coarse-grained (0.05–1.20 mm) (zone I in Fig. 10c), whereas band B is relatively fine-grained (≤0.05 mm) (zone II in Fig. 10c). Additionally, they are characterized by habit and size of the calcite crystals: band A has anhedral elongate crystals of calcite ranging from 0.5–6.0 mm in the direction of the long axis and 0.2–0.5 mm in the direction of the short axis; band B has hexagonal subhedral crystals of calcite ranging from 0.3–1.5 mm; and band C has platy-subhedral crystals of calcite with sizes between 1 and 10 mm. Independently of the textures, the three bands record similar composition: bands A and B are composed of a 70% of the aggregate laumontite + stilbite and a 30% of calcite. Band C, in contact with the host rock, is filled with a 30% of prismatic subhedral-platy calcite, a 65% of an aggregate of subhedral laumontite + stilbite and a 5% of orthopyroxene, likely to come from the host rock. Contact zones between bands A-B and B-C are sharp and nearly straight, and have syntaxial growth of crystals: band B has subhedral platy crystals of laumontite (0.1–2.0 mm) growing perpendicular to the boundary in contact with band A; band C, on the other hand, has crystals of calcite and laumontite growing perpendicular to its boundaries towards the center (e.g. zone I in Fig. 10c). Additionally, bands A and C have intergrowth of calcite and laumontite (e.g. zone III in Fig. 10c), which indicates co-precipitation. Syntaxial growth and intergrowth textures indicate that each one of the three individual bands have formed in three crack-seal episodes (Ramsay, 1980).

4.3.3. Hydrothermal breccia of the ATF specific segment

The representative sample of a hydrothermal breccia in the ATF exposure is composed of two NW-subvertical bands distinguished by mesoscopic color and internal textures (bands A and B in Fig. 11a–c). Band A is white, has a width of 4 mm, and consists of a fine-grained mosaic of subhedral-platy laumontite (≤0.15 mm). Band B is composed of a 40% of white sub-rounded equant clasts (1–3 mm) and a 60% of fine-grained grey matrix of subhedral-platy laumontite (≤0.15 mm). Clasts in band B are composed of smaller clasts of laumontite and quartz (zones II and III in Fig. 11c, d), imbedded in a matrix of fine-grained grey laumontite (≤0.15 mm). Clasts in band B very likely to correspond to fragments of band A, as it becomes evident due to their similarity in mesoscopic color and mineralogy (Fig. 11a). Additionally, bands A and B are cut by: (1) mm-width NW/subvertical veins with curved and diffuse boundaries, composed of relatively large crystals of subhedral-platy syntaxial laumontite (0.5 × 0.2 mm) (Fig. 11c), and (2) N45°W/25°SW tectonic comminution breccias (zone I Fig. 11c, d) (Jébrak, 1997), composed of an 80% of a mixture of angular clasts of laumontite and quartz (characteristic sizes 0.1 mm), imbedded in a 20% of a fine-grained matrix of angular clasts of laumontite (≤0.01 mm).

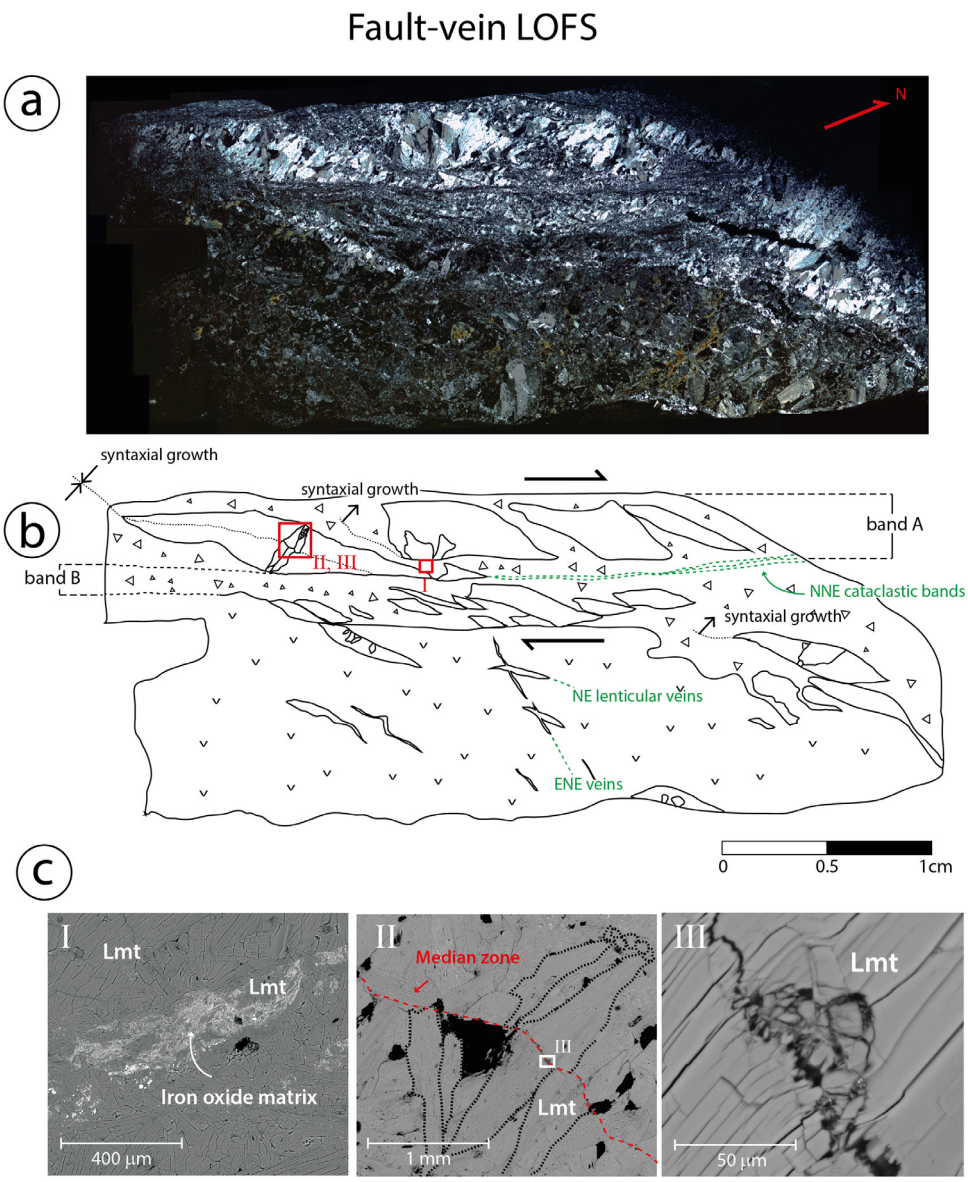

Fig. 9. a) Photomosaic of the horizontal thin section LR7.75 (XPL). This sample corresponds to a fault-vein of the LOFS exposure. b) Microstructural map of the sample. In red, areas observed using SEM; in green, the different structural families defined. Schematic crystals are drawn, along with black arrows, indicating growth direction of the crystals. c) Photomicrographies of selected areas in b (SEM-BSE). Zone I shows the texture of the cataclastic unit. Zone II shows syntaxial growth of laumontite crystals. Zone III shows the median zone between syntaxial laumontite crystals, exhibiting cataclastic fabric. Lmt = Laumontite. (For interpretation of the references to colour in this figure legend, the reader is referred to the web version of this article).

5. Discussion

5.1. Brecciated textures, rupture cycle and tectonic regimes

The LOFS and ATF display simple cores and asymmetric damage zones, with damage concentrated within the hanging wall blocks. Occurrence of more damage has been found on the side of the fault with faster seismic velocities (e.g. Berg and Skar, 2005). This is consistent with determined displacements within the hanging wall blocks during coseismic slip across active normal faults (e.g. Stein et al., 1988).

The dominant fractures within the damage zone of the LOFS exposure are hydrothermal breccias (Fig. 6a), whereas in the ATF outcrop are fault-localized hydrothermal breccias (Fig. 6b).

There are different genetic classifications of fault breccias, of which probably the most influential are Sibson's (1986) and Jébrak's (1997) schemes. Here we used the classification of Jébrak (1997), based on the morphology of the fragments and the particle size distribution as a function of the energy input. Two main types of breccias were distinguished: fluid-assisted breccias and tectonic cominution breccias. Jébrak (1997) states that fluid-assisted breccias are formed by fluctuations in pore fluid pressures, and have high dilation ratio α (defined as the proportion of abundance of matrix with respect to the clasts). On the other hand, tectonic comminution breccias are formed by the progressive shear along slip surfaces, and therefore have low α. For this reason, the classification of the breccias was mainly based on two criteria: the nature of the matrix and dilation of the structure (exotic hydrothermal matrix and high α indicating fluid-assisted brecciation, and autogenous matrix with low α indicating tectonic comminution brecciation). Classification of breccias of the studied faults and its implications in fault zone rupture are discussed in the next sections.

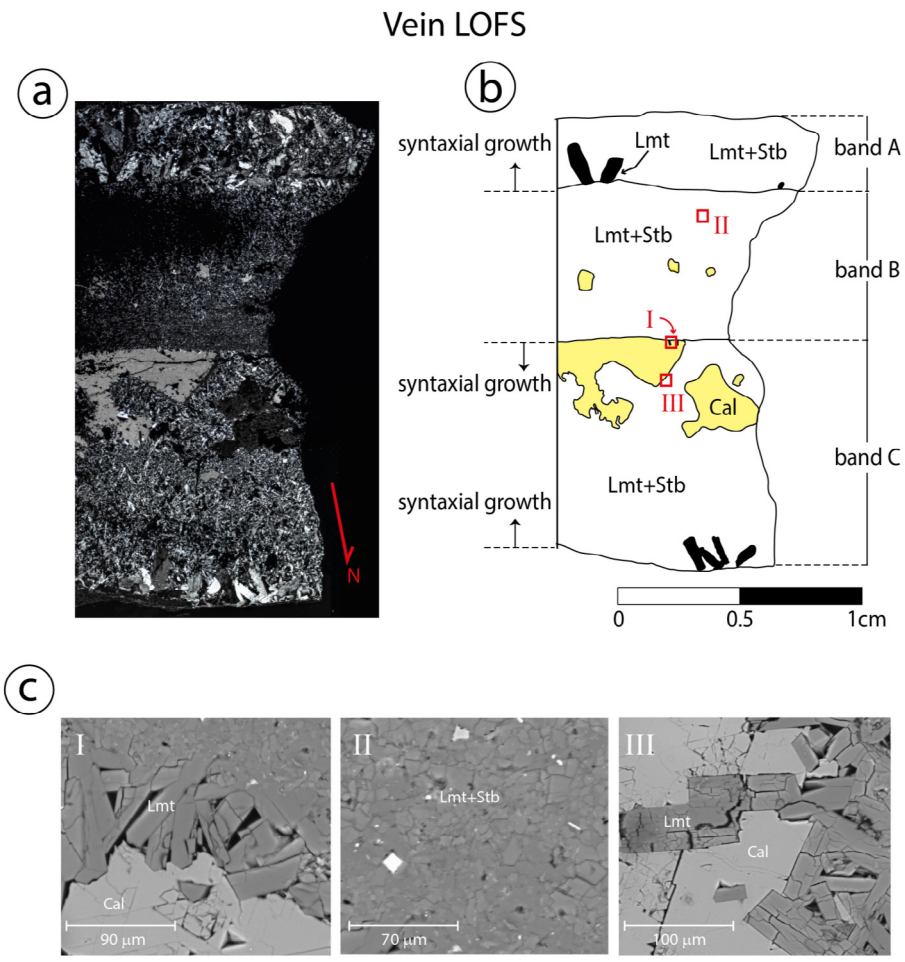

Fig. 10. a) Photomosaic of the horizontal thin section TLR1507 (XPL). This sample corresponds to a banded vein, in contact with the fault core of the LOFS exposure. b) Microstructural map of the sample. In squares, areas observed using SEM. Schematic crystals are drawn, along with black arrows, indicating growth direction of the crystals (black, laumontite crystals; yellow, calcite crystals). c) Photomicrographies of selected areas in b (SEM-BSE). Zone I shows syntaxial growth in the contact between bands B and C. Zone II shows characteristic texture of the fine-grained band B. Zone III intergrowth of calcite and laumontite, indicating co-precipitation. Lmt = Laumontite, Stb = Stilbite, Cal = Calcite. (For interpretation of the references to colour in this figure legend, the reader is referred to the web version of this article).

5.1.1. LOFS splay fault

Hydrothermal breccias in the LOFS outcrop can be classified as fluid-assisted breccias, formed with an important component of extensional (mode I) failure (α = 50-60%). Additionally, at least three extensional (mode I) or hybrid extensional (mode I + II/III) crack-seal episodes can be inferred, as evidenced in the banded vein at the boundary of the core (bands A, B and C in Fig. 10). A conceptual model of the proposed rupture cycle for the LOFS splay fault is shown in Fig. 12a.

The consistency of the suggested rupture cycle can be compared with stress fields obtained in the same studied outcrops in the work done by Pérez-Flores et al. (2016). In the case of the LOFS exposure they obtained a unique Andersonian, strike-slip stress tensor (Table 1). The mode of failure in most of the fractures in the fault zone is in agreement with this stress field: the dominant extensional (mode I) or hybrid extensional (mode I + II/III) fractures (hydrothermal breccias, veins, and vein-faults) mostly occur at 0–30° from the maximum principal stress σ_1. In addition, the least abundant shear (mode II/II) fractures occur at angles that vary between 20–80° from σ_1, and also are compatible with these stress conditions.

5.1.2. ATF specific segment

Fault-localized hydrothermal breccias in the ATF exposure are composed of: (1) a tectonic comminution breccia (α = 5%) (fault in Fig. 6b), and (2) a fluid-assisted breccia (α = 50–60%) (hydrothermal breccia in Fig. 6b), cutting the tectonic comminution breccia. Additionally, another two important observations can be made: field and microstructural evidence demonstrate that the two proposed modes of failure are superimposed (e.g. Figs. 5i, j and 11); and clasts in the fault-localized hydrothermal breccias have, in turn, brecciated texture (zones II and III in Fig. 11). These observations suggest that textures are the result of cyclical rupturing with alternating modes of failure. A conceptual model of the proposed rupture cycle is for the ATF specific segment is shown in Fig. 12b Shear (mode II/III) failure localizes deformation in weakness zones, where a cataclastic fabric is generated (Fig. 12b-i). Extensional (mode I) or hybrid extensional + shear (modes I + II/III) failure produces a transient dilation at such inherited structural sites, conducing to a brecciation of the host rock, circulation of fluids and hydrothermal cementation (Fig. 12b-ii). Subsequent shear (mode II/III) failure may activate the previous fractures and/or produce second-order structures (Fig. 12b-iii).

This rupture cycle is consistent with the work of Pérez-Flores et al. (2016), who obtained two stress tensors: (1) an Andersonian, strike-slip solution; and (2) a non-Andersonian, transtensional solution (Table 1).

The first solution is in good agreement with the mode of failure in most of the fractures. Subvertical shear (mode II/III) fractures (represented in the cataclastic bands within fault-localized

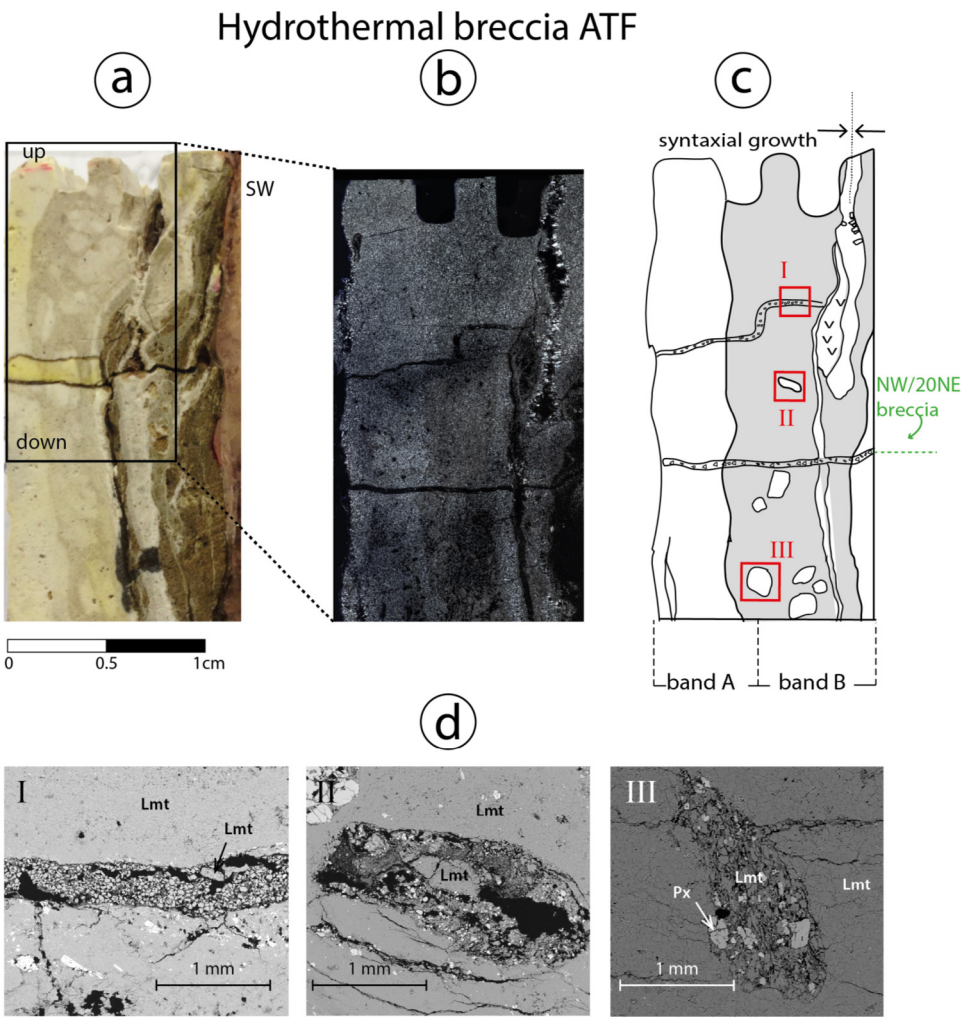

Fig. 11. a) Photography of the vertical sample LAZI7.5E (hydrothermal breccia within the ATF exposure). b) Photomosaic of the vertical thin section LAZI7.5E (XPL). c) Microstructural map of the sample. In squares, areas observed using SEM. Schematic laumontite crystals are drawn, along with black arrows, indicating growth direction of the crystals c) Photomicrographies of selected areas in b (SEM-BSE). Zone I shows a subhorizontal breccia. Zones II and III show characteristic texture of the clasts within band B. Lmt = Laumontite, Px = Pyroxene.

hydrothermal breccias, e.g. Fig. 6b) mostly occur at 30–40° from the maximum principal stress σ_1. Some of the extensional (mode I) or hybrid extensional + shear (modes I + II/III) failure (represented in hydrothermal breccias and veins) respond to the first stress field. In particular, hydrothermal breccias are concentrated at 0–5° from σ_1 and their occurrence is compatible with the presented stress field. However, extensional (mode I) or hybrid extensional + shear (modes I + II/III) fractures (fault-localized hydrothermal breccias, veins and vein-faults) occur at 50–70° from σ_1, which is not compatible with the Andersonian strike-slip regime.

The second solution documents a rotation between σ_1 and σ_2, σ_1 becoming more vertical, which can be associated with the non-Andersonian regime, under particular fluid overpressure conditions discussed later (Section 5.3). Rotation of the stress tensor appears to be the simplest solution related to the reactivation of the studied fractures of the ATF exposure. In fact, mechanical models indicate kinematic switches in the ATF between Andean interseismic (NW-striking faults display sinistral-reverse slip) and Andean co- and postseismic (NW-striking faults are normal-dextral) (Stanton-Yonge et al., 2016), which is associated with changes between gently and steeply-plunging σ_1 at the overriding plate (Hardebeck, 2012).

The proposed rupture model for the ATF is comparable with geological observations in other tectonic contexts (e.g. Dempsey et al., 2014). Extensional/hybrid (mode I, modes I + II/III) reactivation of shear (mode II/III) fractures has been observed to require elevated fluid pressures in zeolite-bearing normal faults, involving an initial stage of fluid ingress, then trapped and overpressured, which leads to fluid-assisted brecciation.

In sum, the previous observations suggest that: (1) the studied local splay fault of the LOFS cyclically fails in transtension under an Andersonian strike-slip regime (i.e. $\sigma_2 \approx \sigma_V$) and (2) the analyzed segment of the ATF records switches in the outcrop-scale stress regimes, changing between failure in transpression under an Andersonian strike-slip regime ($\sigma_2 \approx \sigma_V$) and failure in transtension under a non-Andersonian transtensional regime (i.e. $\sigma_x \neq \sigma_V$, for x = 1, 2, 3).

5.2. Zeolite geothermometry, paleodepth conditions and paleogeothermal gradient

Zeolite P-T experimental stability conditions are in the range of 50–400 °C and 5–25 MPa (Liou et al., 1991). In general, *in situ* temperatures are in fairly good agreement with experimental results (Kristmannsdóttir and Tómasson, 1978; Liou et al., 1987). Therefore, experimental temperature stability intervals have been specially used to study active geothermal systems (e.g. Browne, 1978 and references therein). However, experimental pore fluid

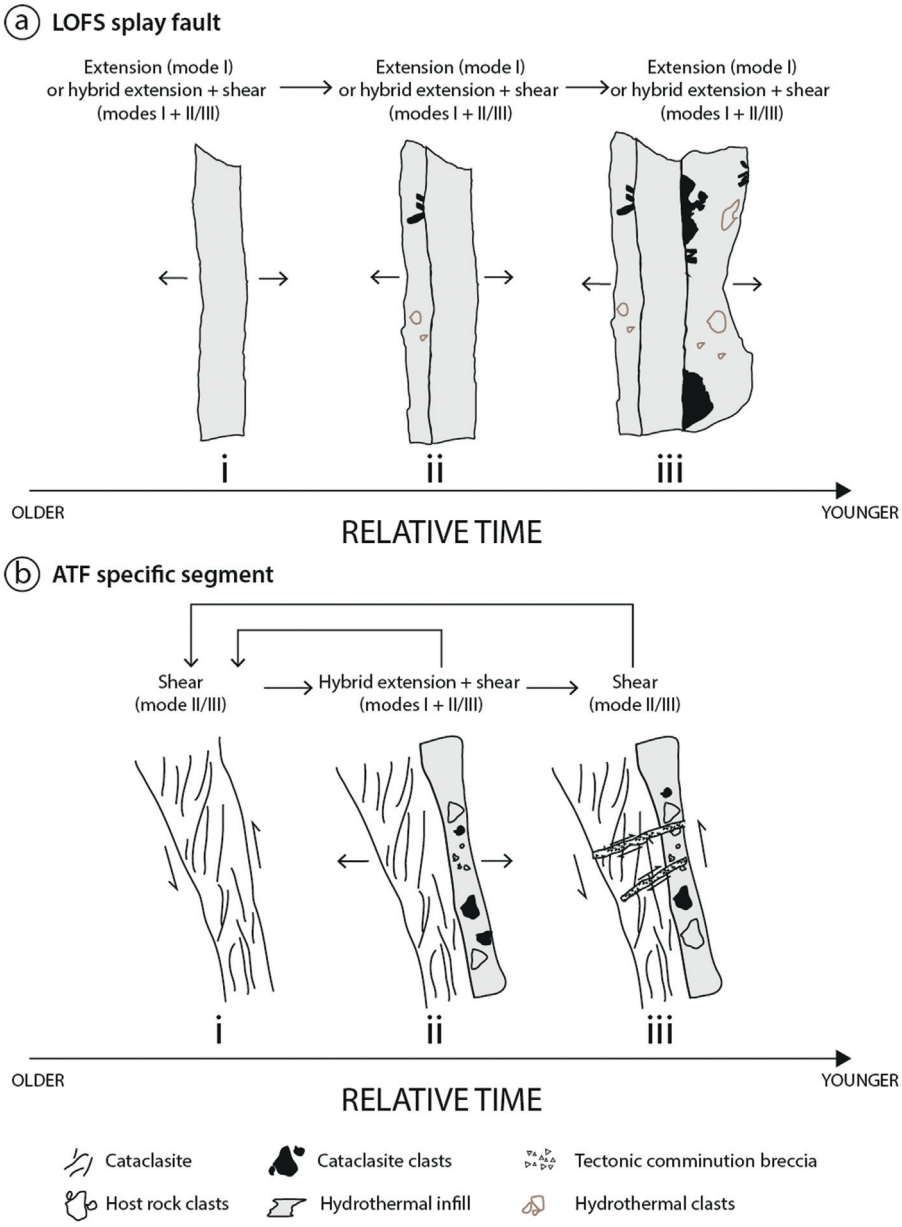

Fig. 12. Proposed rupture cycle for the LOFS and the ATF exposures (cross-section view), based on the inferred modes of failure of the dominant fractures within the damage zones. See text for discussion.

pressures do not account for dynamic pressure effects, not necessarily neglectable in the case of shallow hydrothermal systems (e.g. as indicated in Kristmannsdóttir and Tómasson, 1978). Thus, in this work pore fluid pressures were approximated using the proposed hydromechanical model (cf. Section 5.3).

The dominant minerals detected in the study areas are Ca and Ca(-Na) zeolites (Fig. 7), usually found in hydrothermal systems as a result of the interaction of chloride fluids of near-neutral pH and volcanic rocks (Browne, 1993). Detected mineralogy indicates the dominance of laumontite, the best index mineral for zeolite facies metamorphism (Liou et al., 1991), locally found in the following assemblages: (1) laumontite + stilbite, which indicates crystallization close to 110 °C (in the LOFS exposure); (2) laumontite + scolecite at 120 °C (in the ATF exposure); and (3) laumontite + wairakite, at 210 °C (in the ATF exposure). Moreover, an invariant point at ca. 600 bar and 150 °C has been proposed for the stable coexistence of stilbite, heulandite and laumontite (Cho et al., 1987). In the case of the ATF specific segment, the fact that zeolitic associations indicate temperatures of 120 °C and 210 °C suggests that reaction kinetics is slow enough to allow two metastable associations to coexist. However, following experimental P-T determinations of Liou et al. (1991) and empirical observations of Kristmannsdóttir and Tómasson (1978), the presence of wairakite could suggest that, at least punctually, a high geothermal gradient and P_{H2O}/P_{TOTAL} ratio was reached.

Depth level of exposure at the time of vein formation can be inferred from regional chronostratigraphic observations. Namely, the stratigraphic column of the Curamallín Formation, in which the andesitic host rocks of the LOFS and ATF exposures occur, has been deposited in a segmented intra-arc continental rift basin that reached a total thickness of ~2.5 km (Suárez and Emparan, 1995, 1997; Melnick et al., 2006; Radic, 2010). The Curamallín Formation underlies a Late Miocene hiatus, during which shortening results in inversion of the former basins, uplift and exhumation (Melnick et al., 2006), and therefore deposition may be limited. Directly above, Pliocene-Holocene volcanic rocks occur, with a thickness

< 0.5 km (e.g. Cola de Zorro Formation in González and Vergara, 1962). Therefore, the Curamallín Formation was likely never buried at depths > 3 km. Consistently, fission track studies in Miocene granitoids intruding some of our vein's host rocks (ca. 38°45′S) (Fig. 2), indicate paleodepths ca. 4 km (Glodny et al., 2008).

Assuming that suggested temperature stability intervals from zeolite geothermometry are a good estimation (110°C–210°C), indicated paleodepths for host rocks (< 3 km) imply minimum paleogeothermal gradients in the range of 30–70 °C/km. Such values are in agreement with gradients found in geothermal areas, typically > 25–50 °C (*e.g.* Aldrich et al., 1981).

5.3. Failure envelope and conditions for brittle failure

Here we take a quantitative approach, combining geological observations and mechanical models. We use the dominant modes of failure recorded in the studied sites and compare them to specific hydromechanical conditions in $\lambda - \sigma$ space.

We modeled the Andersonian strike-slip regimes using Cox's (2010) scheme. To depict these graphs we used: (1) the maximum depth inferred from chronostratigraphic observations (< 3 km in 0.5 km intervals); (2) a representative coefficient of internal friction $\mu = 0.75$ (considering that rocks at elevated temperature gradients often seal and regain cohesive strength on timescales of rupture recurrence, following Cox, 2005); (3) a representative value of *in-situ* tensile strength T = 5 MPa (following Gudmundsson, 2011); and (4) a density of $\rho = 2450\ kg/m^3$ (expected for an andesite, following Rowland and Sibson, 2004).

To model failure conditions in the non-Andersonian transtensional regime, we extended the analysis to a general case, considering the reactivation of previously existing fractures, in which σ_2 is not necessarily contained on the plane of the inherited structure. For this reason, the method allows to study extremely complex structural settings, incorporating the effect of any rotation of the principal stresses with respect to an inherited anisotropy (cf. section 3.2). Generalized non-Andersonian $\lambda - \sigma$ diagrams were obtained projecting the principal stresses in Table 1 on a representative fault-localized hydrothermal breccia (N45°W/80°SW) (cf. sections 5.1.1 and 5.1.2). Depths and mechanical properties are the same as those of the Andersonian case.

Results of the Andersonian and non-Andersonian models are shown in Fig. 13a, b. Cold hydrostatic and lithostatic pore fluid factors are shown for reference. Typical overpressures in active geothermal areas (40–48% lithostatic pressure) (Rowland and Simmons, 2012), which can be taken as a representative minimum fluid pressure, are also depicted for reference.

The graphs illuminate about some important points in the hydromechanical conditions of the studied outcrops (Fig. 13a, b):

1) Differential stresses acting on seismogenic planes subject to fluid overpressure have been inferred to satisfy the relationship $\sigma_1 - \sigma_3 = 4T$ (Gudmundsson, 1999). Using T = 5 MPa, differential stresses might roughly be 20 MPa. This value compares well to differential stresses associated with points of transition between shear (mode II/III) and hybrid extension + shear (modes I + II/III) (28–20 MPa).
2) Independently of the depth and failure mode, for a given differential stress, fluid pressures from non-Andersonian models are higher than in Andersonian models. Moreover, transitions between failure in shear (mode II/III) and hybrid extension + shear (modes I + II/III) in Andersonian and non-Andersonian models occur at comparable differential stresses. Additionally, these transitions occur at higher fluid pressures in the non-Andersonian cases. Nevertheless, at shallow structural levels, increase in the fluid pressures is greater than in deeper levels. For example, for 1.5 km depth fluid pressures changes from 60% to 95% lithostatic, whereas for 3 km fluid pressures changes from 85% to 98% lithostatic, at both depths with modest change in differential stress (28–20 MPa).
3) Consequently, in the studied ATF segment, fluid pressures need to increase to fail in the non-Andersonian regime.
4) On the other hand, in the Andersonian models, failure in the LOFS splay fault is consistent with extensional (mode I) or extensional + shear (modes I + II/III) failure at < 28 MPa and > 40–80% lithostatic.

5.4. Fault-controlled development of shallow hydrothermal systems

Multi-scale structural analyses suggest that the fundamental mechanical principles governing fault zone behavior remain scale-invariant, at least between the mm and the km scale (e.g. Kim and Sanderson, 2004; Jensen et al., 2011). Assuming the observed meso- and microstructural features can extrapolate to a regional behavior, a proposed mechanism for the development of shallow hydrothermal systems in northern end of the LOFS is summarized in Fig. 14.

The N83°W/65°S local splay fault of the LOFS seems to accommodate the Andersonian tensor apparently coupled with long-term stress conditions of Andean interseismic (Pérez-Flores et al., 2016; Stanton-Yonge et al., 2016), representing subsidiary EW-striking faults of the LOFS. Continuous fluid flow through EW to NE-striking fractures seems to develop under these conditions (Fig. 14). Such fractures are favorably oriented for failure in extension (mode I) or hybrid extension + shear (modes I + II/III) at fluid pressures > 40–80% lithostatic. The idea of cyclical failure is supported by textural features summarized in Section 5.1.

The N45°W/60°SW segment of the ATF is severely misoriented for extensional (mode I) or hydrid extensional + shear (modes I + II/III) failure in the Andersonian tensor. However, shear (mode II/III) failure in NW-striking structures may be induced at fluid pressures < 40–80% lithostatic. Such a scenario could promote the generation of fault-controlled compartments (e.g. below the gently-dipping tectonic comminution breccia in Fig. 11), which may facilitate the storage hydrothermal fluids. This might ultimately build-up fluid pressures for reactivation of NW-striking fractures in hybrid extension + shear (mode I + II/III) at anomalously high fluid pressures (>85–98% lithostatic) in the non-Andersonian regime (Fig. 14). The existence of fault-controlled compartments associated with the ATF has also been inferred by other authors (Cembrano and Lara, 2009; Sánchez et al., 2013; Pérez-Flores et al., 2016; Sánchez-Alfaro et al., 2016; Tardani et al., 2016), who suggest that NW to WNW-striking faults of the ATF could promote long-term residence of magma and hydrothermal fluids. Non-Andersonian regimes might be associated with Andean co- and postseimic, in which a quasi-instantaneous relaxation of the continental plate occurs after a subduction megathrust earthquake, as already inferred in crustal intra-arc and fore-arc faults within the Andean margin (e.g. González et al., 2003; Farías et al., 2011; Aron et al., 2010; Stanton-Yonge et al., 2016).

Finally, we conclude that long-term stress conditions favor: (1) the storage of hydrothermal fluids in reservoirs associated with the NW-striking faults of the ATF and (2) continuous fluid flow through vertical high-flux conduits in the EW-striking faults of the LOFS. The interplay between the studied faults allows one of the basic requirements for the development of shallow hydrothermal systems: an architecture that permits the transportation of previously stored hydrothermal fluids. These results suggest that areas of spatial interaction between the ATF and LOFS are structurally ideal places for concentrated hydrothermal activity. However, the occurrence hydrothermal systems might not be exclusively spatially-related to fault intersections, as evidenced by locally present fumaroles

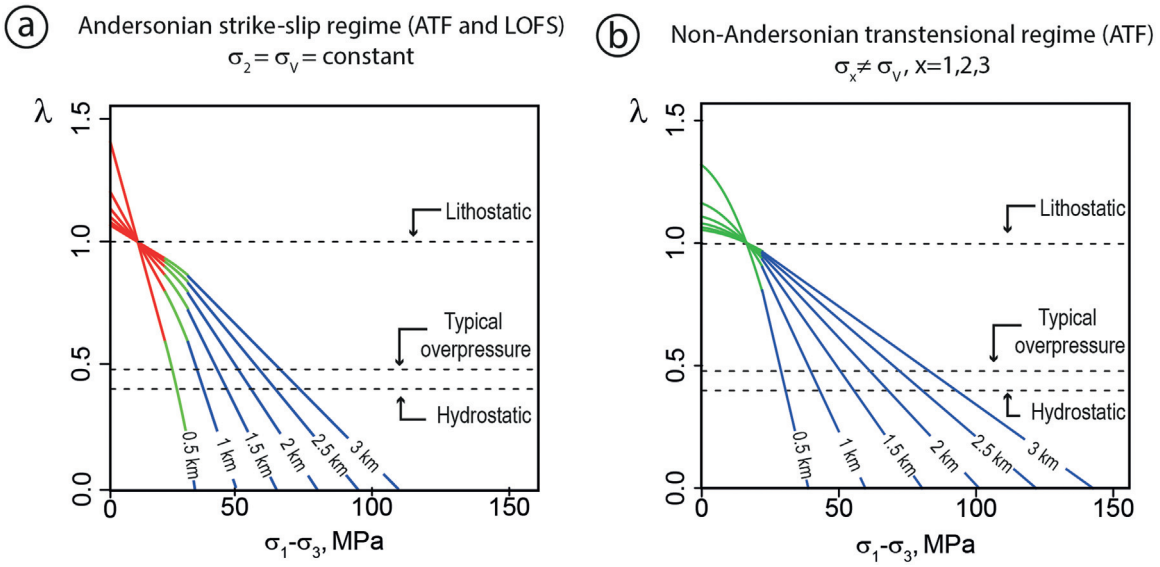

Fig. 13. a) Andersonian strike-slip λ – σ diagram. Such regime was inferred to act in both the LOFS and ATF exposures b) Non-Andersonian transtentional λ – σ diagram, only present in the ATF exposure. Failure curves are color-coded: red = extension (mode I), green = extension + shear (modes I + II/III), blue = shear (mode II/III). Cold hydrostatic and lithostatic pore fluid factors are depicted, along with typical overpressures in active geothermal areas (Taupo Volcanic Zone, 40–48% lithostatic pressure) (Rowland and Simmons, 2012). See text for discussion. (For interpretation of the references to colour in this figure legend, the reader is referred to the web version of this article).

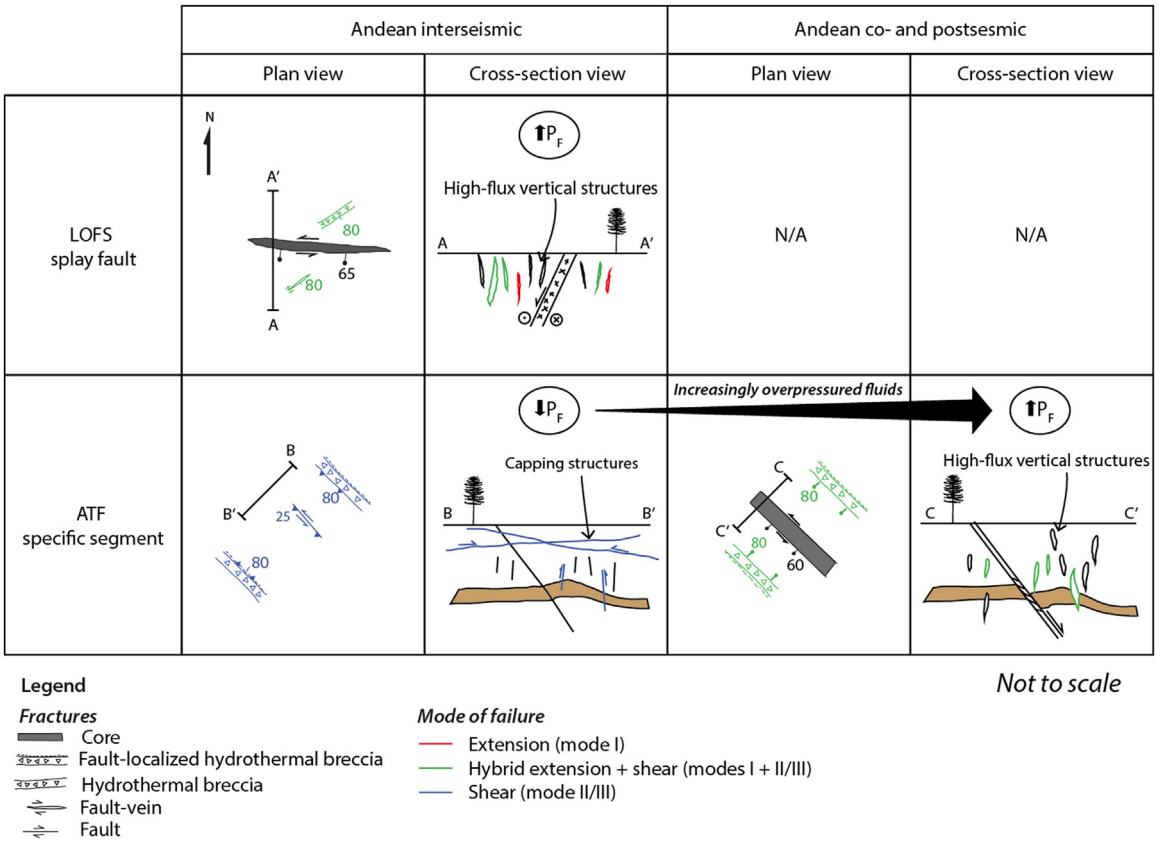

Fig. 14. Conceptual model of the formation of shallow hydrothermal systems in the Southern Andes. The LOFS exposure registers continuous fluid flow through NE to EW-striking extensional (mode I) or hybrid extensional + shear (modes I + II/III) fractures under long-term stress conditions (Andean interseismic). The behavior during Andean co/postseismic is not registered in the studied exposure. On the other hand, the ATF segment records a switch in the tectonic regime. Failure in shear (mode II/III) probably occurs during long-term stress conditions of Andean interseismic. Such a scenario could promote the storage of increasingly overpressured fluids under capping structures, facilitating expulsions in large volumes during switches to failure in hybrid extension + shear (modes I + II/III), during Andean co/postseismic phases. See text for further discussion. (For interpretation of the references to colour in this figure legend, the reader is referred to the web version of this article).

and hot springs (e.g. Tardani et al., 2016). Therefore, this work is a first approach for understanding the complex dynamics of Andean hydrothermal systems and its relationship with potential geothermal reservoirs.

6. Conclusions

The Liquiñe-Ofqui Fault System (LOFS) and the Andean Transverse Faults (ATF) were studied from the outcrop to the microscopic scale, based on its textural, mineralogical and structural characteristics. The main conclusions of this work are:

1) Architectural features in the studied exposures suggest that the analyzed local splay fault of the LOFS cyclically fails in transtension under an Andersonian strike-slip regime (i.e. $\sigma_2 \approx \sigma_V$). On the other hand, the studied segment of the ATF records switches in the outcrop-scale stress regimes, changing between failure in transpression under an Andersonian strike-slip regime ($\sigma_2 \approx \sigma_V$) and failure in transtension under a non-Andersonian transtensional regime (i.e. $\sigma_X \neq \sigma_V$, for x = 1, 2, 3).
2) The dominant minerals detected through XRD in the study areas are Ca and Ca(-Na) rich zeolites, found in geothermal systems as a result of the interaction of chloride hydrothermal fluids of near-neutral pH and volcanic rocks. Syntectonic zeolites in the damage zones of the LOFS and the ATF exposures indicate minimum paleogeothermal gradients in the range of 30–70 °C/km.
3) Modeled failure envelopes in $\lambda - \sigma$ space indicate that for 0.5–3.0 km, the ATF segment fails in shear (mode II/III) at differential stresses > 28 MPa and fluid pressures < 40–80% lithostatic, in the Andersonian regime. Although failure in hybrid extension + shear (modes I + II/III) at the ATF segment occurs at comparable differential stresses (< 20 MPa), fluid pressures need to increase up to > 85–98% lithostatic in the non-Andersonian stress regime. In the LOFS exposure, failure occurs in extension (mode I) or hybrid extension + shear (modes I + II/III), at differential stresses < 28 MPa and fluid pressures > 40–80%, in the Andersonian stress regime.
4) Long-term stress conditions are related to the Andersonian stress regime, which favors continuous fluid flow in the EW-striking splay faults of the LOFS. On the other hand, quasi-instantaneous relaxation of the continental plate is related to the non-Andersonian stress regime, which allows sporadic failure associated with anomalously overpressured fluids in the ATF. This suggests that fault-controlled compartments related to the ATF need to accumulate and build up fluid pressures during long-term Andersonian stress conditions. Since hydrothermal systems require an architecture that both accumulates and transports hydrothermal fluids, this could be specially favored in areas of spatial interaction between the NW-striking and EW-striking faults of the ATF and LOFS, respectively. This first-order structural control must be taken into consideration for further development and prospecting of geothermal reservoirs in the Southern Andes.

Acknowledgements

This work is a contribution to the Centro de Excelencia en Geotermia de los Andes (CEGA–FONDAP/CONICYT Project #15090013) and the FONDECYT Project #1130030. This manuscript was improved during an internship funded by the International Cooperation Project CONICYT REDES #140036. TR thanks Martin Reich for all his support. The authors thank Patrick Browne for comments in the petrographic analysis. Mercedes Vázquez, Estefanía Terrón and Fabián Tapia are also thanked for the XRD data acquisition and interpretation. Field work was carried out with the help of Juan Ignacio Sánchez, Pamela Pérez-Flores and Pablo Sánchez-Alfaro. Authors thank Sara Elgueta for comments in chronostratigraphic features. Finally, we thank the comments of three anonymous referees for their comments that improved of the quality of this manuscript, and the editor-in-chief Eva Schill for the valuable help during the review process.

References

Aldrich, M.J., Laughlin, A.W., Gambill, D.T., 1981. Geothermal resource base of the world: a revision of the Electric Power Research Institute's estimate. In: Tech. rep. Los Alamos Scientific Laboratory, University of California, pp. 64.
Anderson, E.M., 1905. The dynamics of faulting. Trans. Edinburgh Geol. Soc. 8 (3), 387–402.
Arancibia, G., Cembrano, J., Lavenu, A., 1999. Transpresión dextral y partición de la deformación en la Zona de Falla Liquiñe-Ofqui, Aisén, Chile (44–45 °S). Rev. Geol. Chile 26 (1), 03–22.
Aron, F., Allmendinger, R.W., Cembrano, J., González, G., Yáñez, G., 2010. 2013. Permanent foreárc extension and seismic segmentation: Insights from the Maule earthquake, Chile. J. Geophys. Res. Sol. Earth 118 (2), 724–739.
Berg, S.S., Skar, T., 2005. Controls on damage zone asymmetry of a normal fault zone: outcrop analyses of a segment of the Moab fault, SE Utah. J. Struct. Geol. 27 (10), 1803–1822.
Bons, P.D., Elburg, M.A., Gomez-Rivas, E., 2012. A review of the formation of tectonic veins and their microstructures. J. Struct. Geol. 43, 33–62.
Browne, P., 1978. Hydrothermal alteration in active geothermal fields. Annu. Rev. Earth Planet. Sci. 6, 229–250.
Browne, P., 1993. Application of Mineralogical Methods to assess the Thermal Stabilities of Geothermal Reservoirs. Proceedings of the Eighteenth Workshop on Geothermal Reservoir Engineering. Paper no. 145, 6.
Cembrano, J., Hervé, F., Lavenu, A., 1996. The Liquiée Ofqui fault zone: a long-lived intra-arc fault system in southern Chile. Tectonophysics 259 (1), 55–66.
Cembrano, J., Lara, L., 2009. The link between volcanism and tectonics in the southern volcanic zone of the Chilean Andes: a review. Tectonophysics 471 (1), 96–113.
Cho, M., Maruyama, S., Liou, J.G., 1987. An experimental investigation of heulandite-laumontite equilibrium at 1000–2000 bar P fluid. Contrib. Mineral. Petrol. 97 (1), 43–50.
Cole, J.W., 1990. Structural control and origin of volcanism in the Taupo volcanic zone, New Zealand. Bull. Volcanol. 52 (6), 445–459.
Cox, S., 2005. Coupling between deformation, fluid pressures, and fluid flow in ore-producing hydrothermal systems at depth in the crust. Econ. Geol., 39–75.
Cox, S., 2010. The application of failure mode diagrams for exploring the roles of fluid pressure and stress states in controlling styles of fracture-controlled permeability enhancement in faults and shear zones. Geofluids 10 (12), 217–233.
Dahlen, F.A., 1984. Noncohesive critical Coulomb wedges: an exact solution. J. Geophys. Res. 89 (B12), 10125–10133.
Dempsey, E.D., Holdsworth, R.E., Imber, J., Bistacchi, A., Di Toro, G., 2014. A geological explanation for intraplate earthquake clustering complexity: the zeolite-bearing fault/fracture networks in the Adamello Massif (Southern Italian Alps). J. Struct. Geol 66, 58–74.
Farías, M., Comte, D., Roecker, S., Carrizo, D., Pardo, M., 2011. Crustal extensional faulting triggered by the 2010 chilean earthquake: the pichilemu seismic sequence. Tectonics 30 (6).
Faulkner, D.R., Lewis, A.C., Rutter, E.H., 2003. On the internal structure and mechanics of large strike-slip fault zones: field observations of the Carboneras fault in southeastern Spain. Tectonophysics 367 (3), 235–251.
Faulkner, D., Jackson, C., Lunn, R.J., Schlische, R.W., Shipton, Z.K., Wibberley, C.A.J., Withjack, M.O., 2010. A review of recent developments concerning the structure, mechanics and fluid flow properties of fault zones. J. Struct. Geol. 32 (11), 1557–1575.
Folguera, A., Ramos, V.A., Melnick, D., 2002. Partición de la deformación en la zona del arco volcánico de los Andes neuquinos (36–39°S) en los últimos 30 millones de años. Rev. Geol. Chile 29 (2), 227–240.
Gillespie, P.A., Howard, C.B., Walsh, J.J., Watterson, J., 1993. Measurement and characterization of spatial distributions of fractures. Tectonophysics 226 (1–4), 113–141.
Glodny, J., Gräfe, K., Echtler, H., Rosenau, M., 2008. Mesozoic to Quaternary continental margin dynamics in south-central Chile (36–42°S): The apatite and zircon fission track perspective. Int. J. Earth Sci. 97 (6), 1271–1291.
González, O., Vergara, M., 1962. Reconocimiento geológico de la Cordillera de los Andes entre los paralelos 35° y 38° latitud sur, Univ. Chile. Inst. Geol. 24, 119.
González, G., Cembrano, J., Carrizo, D., Macci, A., Schneider, H., 2003. The link between forearc tectonics and Pliocene–Quaternary deformation of the Coastal Cordillera, northern Chile. J. S. Am Earth Sci. 16 (5), 321–342.
Gudmundsson, A., 1999. Fluid overpressure and stress drop in fault zones. Geophys. Res. Lett. 26 (1), 115–118.
Gudmundsson, A., 2011. Rock fractures in geological processes. Cambridge University Press, pp. 570.
Hafner, W., 1951. Stress distributions and faulting. Geol. Soc. Am. Bull. 62 (4), 373–398.

Hardebeck, J.L., 2012. Coseismic and postseismic stress rotations due to great subduction zone earthquakes. Geophys. Res. Lett. 39 (21).
Hashimoto, Y., Eida, M., 2015. Quantitative estimation of fluid pressure ratio of shear vein in a on-land accretionary complex, the Yokonami mélange, the Cretaceous Shimanto Belt, Kochi, southwest Japan. Tectonophysics 665, 17–22.
Hubbert, M.K., Rubey, W.W., 1959. Role of fluid pressure in mechanics of overthrust faulting. Part 1. Geol. Soc. Am. Bull. 62, 355–372.
Jébrak, M., 1997. Hydrothermal breccias in vein-type ore deposits: a review of mechanisms, morphology and size distribution. Ore Geol. Rev. 12 (3), 111–134.
Jaeger, J.C., Cook, N.G.W., 1979. Fundamentals of rock mechanics. Chapman & Haii, pp. 379.
Jensen, E., Cembrano, J., Faulkner, D., Veloso, E., Arancibia, G., 2011. Development of a self-similar strike-slip duplex system in the Atacama Fault system, Chile. J. Struct. Geol. 33 (11), 1611–1626.
Kim, Y.S., Sanderson, D.J., 2004. Similarities between strike-slip faults at different scales and a simple age determining method for active faults. Isl. Arc. 13 (1), 128–143.
Kristmannsdóttir, H., Tómasson, J., 1978. Zeolite zones in geothermal areas in Iceland. Nat. Zeolites Occur. Prop. Use, 277–284.
Krupp, R.E., Seward, T.M., 1987. The Rotokawa geothermal system, New Zealand; an active epithermal gold-depositing environment. Econ. Geol. 82 (5), 1109–1129.
Lange, D., Cembrano, J., Rietbrock, A., Haberland, C., Dahm, T., Bataille, K., 2008. First seismic record for intra-arc strike-slip tectonics along the Liquiñe?Ofqui fault zone at the obliquely convergent plate margin of the southern Andes. Tectonophysics 455 (1–4), 14–24.
Lavenu, A., Cembrano, J., 1999. Compressional-and transpressional-stress pattern for Pliocene and Quaternary brittle deformation in fore arc and intra-arc zones (Andes of Central and Southern Chile). J. Struct. Geol. 21 (12), 1669–1691.
Liou, J.G., Maruyama, S., Cho, M., 1987. Very low-grade metamorphism of volcanic and volcaniclastic rocks-mineral assemblages and mineral facies. Low Temp. Metamorph. 59, 113.
Liou, J.G., de Capitani, C., Frey, M., 1991. Zeolite equilibria in the system $CaAl_2Si_2O_8$–$NaAlSi_3O_8$–SiO_2–H_2O. N. Z. J. Geol. Geophys. 34 (3), 293–301.
Melnick, D., Rosenau, M., Folguera, A., Echtler, H., 2006. Neogene tectonic evolution of the Neuquén Andes western flank (37–39°S). Geol. S. Am. S. 407, 73–95.
Moreno, M., Melnick, D., Rosenau, M., Bolte, J., Klotz, J., Echtler, H., Baez, J., et al., 2011. Heterogeneous plate locking in the South–Central Chile subduction zone: building up the next great earthquake. Earth Planet. Sci. Lett. 305 (3–4), 413–424.
Morris, A., Ferrill, D.A., Henderson, D.B., 1996. Slip-tendency analysis and fault reactivation. Geology 24 (3), 275–278.
Olson, J.E., Pollard, D.D., 1991. The initiation and growth of en échelon veins. J. Struct. Geol. 13 (5), 595–608.
Pérez-Flores, P., Cembrano, J., Sánchez-Alfaro, P., Veloso, E., Arancibia, G., Roquer, T., 2016. Tectonics, magmatism and paleo-fluid distribution in a strike-slip setting: insights from the northern termination of the Liquiñe – Ofqui fault System, Chile. Tectonophysics 680, 192–210.
Peacock, D.C.P., Nixon, C.W., Rotevatn, A., Sanderson, D.J., Zuluaga, L.F., 2016. Glossary of fault and other fracture networks. J. Struct. Geol. 92, 12–29.
Radic, J.P., 2010. Las cuencas cenozoicas y su control en el volcanismo de los Complejos Nevados de Chillan y Copahue-Callaqui (Andes del Sur, 36–39°S). Andean Geol. 37 (1), 220–246.
Ramsay, J.G., 1980. The crack–seal mechanism of rock deformation. Nature 284, 135–139.
Reuther, C.D., Potent, S., Bonilla, R., 2003. Crustal stress history and geodynamic processes of a segmented active plate margin: South-Central Chile: the Arauco Bío-Bío trench arc system. 10th Chilean Geological Congress, 11.
Rivera, O., Cembrano, J., 2000. Modelo de formación de cuencas volcano-tectónicas en zonas de transferencia oblicuas a la cadena andina: el caso de las cuencas oligo-miocénicas de Chile central y su relación con estructuras NWW-NW (33°00'-34°30'S). 9th Chilean Geological Congress, 5.
Rivera, O., Yáñez, G., 2009. Naturaleza y rol de estructuras translitosféricas en la evolución del arco volcánico oligo-mioceno de Chile Central entre los 32 y 34°S. 2nd Chilean Geological Congress, 1.
Rosenau, M., Melnick, D., Echtler, H., 2006. Kinematic constraints on intra-arc shear and strain partitioning in the southern Andes between 38°S and 42°S latitude. Tectonics 25 (4).
Rowland, J., Sibson, R.H., 2004. Structural controls on hydrothermal flow in a segmented rift system, Taupo Volcanic Zone, New Zealand. Geofluids 4 (4), 259–283.
Rowland, J., Simmons, S.F., 2012. Hydrologic, magmatic, and tectonic controls on hydrothermal flow, Taupo Volcanic Zone, New Zealand: implications for the formation of epithermal vein deposits. Econ. Geol. 107 (3), 427–457.
Sánchez, P., Pérez-Flores, P., Arancibia, G., Cembrano, J., Reich, M., 2013. Crustal deformation effects on the chemical evolution of geothermal systems: the intra-arc Liquiáe–Ofqui fault system, Southern Andes. Int. Geol. Rev. 55 (11), 1384–1400.
Sánchez-Alfaro, P., Reich, M., Arancibia, G., Pérez-Flores, P., Cembrano, J., Driesner, T., Lizama, M., et al., 2016. Physical, chemical and mineralogical evolution of the Tolhuaca geothermal system, southern Andes, Chile: insights into the interplay between hydrothermal alteration and brittle deformation. J. Volcanol. Geotherm. Res. 324, 88–104.
Salfity, J.A., 1985. Lineamentos transversales al rumbo andino en el Noroeste Argentino. 4th Chilean Geological Congress.
Secor, D.T., 1965. Role of fluid pressure in jointing. Am. J. Sci. 263 (8), 633–646.
Sibson, R.H., 1986. Brecciation processes in fault zones: inferences from earthquake rupturing. Pure Appl. Geophys 124 (1-2), 159–175.
Sibson, R.H., 1998. Brittle failure mode plots for compressional and extensional tectonic regimes. J. Struct. Geol. 20 (5), 655–660.
Sibson, R.H., 2003. Thickness of the seismic slip zone. Bull. Seismol. Soc. Am. 93 (3), 1169–1178.
Sibson, R.H., 2004. Controls on maximum fluid overpressure defining conditions for mesozonal mineralisation. J. Struct. Geol. 26 (6), 1127–1136.
Simpson, C., Schmid, S., 1983. An evaluation of criteria to deduce the sense of movement in sheared rocks. Geol. Soc. Am. Bull. 94 (11), 1281–1288.
Somoza, R., Ghidella, M.E., 2005. Convergencia en el margen occidental de América del Sur durante el Cenozoico: subducción de las placas de Nazca, Farallón y Aluk. Rev. la Asoc. Geológica Argentina 60 (4), 797–809.
Stanton-Yonge, A., Griffith, W.A., Cembrano, J., St Julien, R., Iturrieta, P., 2016. Tectonic role of margin-parallel and margin-transverse faults during oblique subduction in the Southern Volcanic Zone of the Andes: Insights from Boundary Element Modeling. Tectonics 35 (9), 1990–2013.
Stein, R.S., King, G.C., Rundle, J., 1988. The growth of geological structures by repeated earthquakes, 2: Field examples of continental dip-slip faults. J. Geophys. Res. 93, 13319–13331.
Suárez, M., Emparan, C., 1988. Geocronología y asociación de facies volcánicas y sedimentarias del Mioceno de Lonquimay, Chile (Lat. 38-39°S). 5th Chilean Geological Congress, 365–383.
Suárez, M., Emparan, C., 1995. The stratigraphy, geochronology and paleophysiography of a Miocene fresh-water interarc basin, southern Chile. J. South Am. Earth Sci 8 (1), 17–31.
Suárez, M., Emparan, C., 1997. Hoja Curacautín, Regiones de la Araucanía y del Bío-bío, Serv. Nac. Geol. y Minería. Geological map 1:250.000.
Tardani, D., Reich, M., Roulleau, E., Takahata, N., Sánchez-Alfaro, P., Sano, Y., Pérez-Flores, P., Sánchez-Alfaro, P., Cembrano, J., Arancibia, G., 2016. Exploring the structural controls on helium, nitrogen and carbon isotope signatures in hydrothermal fluids along an intra-arc fault system. Geochim. Cosmochim. Acta. 184, 193–211.
Taylor, G.K., Grocott, J., Pope, A., Randall, D.E., 1998. Mesozoic fault systems, deformation and fault block rotation in the Andean forearc: a crustal scale strike-slip duplex in the Coastal Cordillera of northern Chile. Tectonophysics 299 (1), 93–109.
Tenthorey, E., Cox, S., Todd, H.F., 2003. Evolution of strength recovery and permeability during fluid–rock reaction in experimental fault zones. Earth Planet. Sci. Lett. 206 (1–2), 161–172.
Whitney, D.L., Evans, B.W., 2010. Abbreviations for names of rock-forming minerals. Am. Miner. 95 (1), 185–187.
Wilson, C.J.L., 1994. Crystal growth during a single-stage opening event and its implications for syntectonic veins. J. Struct. Geol. 16 (9), 1283–1296.
Woodcock, N.H., Mort, K., 2008. Classification of fault breccias and related fault rocks. Geol. Mag. 145 (3), 435–440.
Yamaji, A., 2000. The multiple inverse method: a new technique to separate stresses from heterogeneous fault-slip data. J. Struct. Geol. 22 (4), 441–452.
Yin, Z., Ranalli, G., 1992. Critical stress difference, fault orientation and slip direction in anisotropic rocks under non-Andersonian stress systems. J. Struct. Geol. 14 (2), 237–244.
Yin, A., 1989. Origin of regional, rooted low-angle normal faults: a mechanical model and its tectonic implications. Tectonics 8 (3), 469–482.